Large-Scale Nonlocality in "Doubly Special Relativity" with an Energy-Dependent Speed of Light[¶]

R. Schützhold and W. G. Unruh

Canadian Institute for Advanced Research Cosmology and Gravity Program, Department of Physics and Astronomy,
University of British Columbia, Vancouver, V6T 1Z1 Canada
e-mail: schuetz@physics.ubc.ca; unruh@physics.ubc.ca
Received September 1, 2003

There are two major alternatives for violating the (usual) Lorentz invariance at large (Planckian) energies or momenta—either not all inertial frames (in the Planck regime) are equivalent (e.g., there is an effectively preferred frame) or the transformations from one frame to another are (nonlinearly) deformed ("doubly special relativity"). We demonstrate that the natural (and reasonable) assumption of an energy-dependent speed of light in the latter method goes along with violations of locality/separability (and even translational invariance) on macroscopic scales. © *2003 MAIK "Nauka/Interperiodica".*

PACS numbers: 03.30.+p; 11.30.Cp; 04.60.-m

1. Introduction. The observation that there is no invariant energy (or length, etc.) scale in special relativity, on the one hand, and the expected physical significance of the Planck scale, on the other hand, has motivated the suggestion that the (usual) Lorentz invariance might be broken at large (Planckian) energies [1–7]. It has also been suggested [1–10] that several yet unexplained observations, such as the indications for ultrahigh energy cosmic rays (UHECR) with energies above the Greisen–Zatsepin–Kuzmin (GZK) cutoff [11, 12] of order $\mathbb{O}(10^{19}\,\text{eV})$ induced by the interaction with the cosmic microwave background, could be interpreted as empirical evidence for deviations from the Lorentz invariance at high energies. Furthermore, variable speed-of-light (VSL) cosmologies [13, 14], which also require breaking the local Poincaré symmetry, have been considered as alternative solutions of the cosmological problems, which lead to the idea of inflation. In particular, in the first case, one needs to explain the apparent large gap between the energy range of those phenomena $\mathbb{O}(10^{19}\,\text{eV})$ and the Planck scale $\mathbb{O}(10^{28}\,\text{eV})$, but we are not going to discuss these phenomenological issues here (for phenomenological constraints on Lorentz violation, see, e.g., [15, 16] and references therein, cf. [17]).

There are two major alternatives for breaking the Lorentz invariance: either not all inertial frames (in the Planck regime) are equivalent (e.g., there is an effectively preferred frame) or the transformations from one frame to another are different (deformed). In the following paper, we shall consider the second possibility in more detail and discuss some consequences which arise thereof. For the sake of simplicity (and since the

masses of all known "elementary" particles are small compared to Planck scale), we shall only consider massless particles, such as photons. In addition, we shall work in $1 + 1$ dimensions (unless otherwise noted).

The main idea of doubly special relativity (DSR; see, e.g., [1–7, 18]) is to replace the usual linear Lorentz transformation $\mathscr{L}$ by the following nonlinear representation $F \circ \mathscr{L} \circ F^{-1}$, i.e.,

$$\begin{pmatrix} E \\ p \end{pmatrix} \longrightarrow \begin{pmatrix} E' \\ p' \end{pmatrix} = F \circ \mathscr{L} \circ F^{-1} \begin{pmatrix} E \\ p \end{pmatrix}$$

$$= F \left[\frac{\begin{pmatrix} 1 & v \\ v/c^2 & 1 \end{pmatrix}}{\sqrt{1 - v^2/c^2}} F^{-1} \begin{pmatrix} E \\ p \end{pmatrix} \right], \tag{1}$$

with some nonlinear function $F: \mathbb{R}^2 \longrightarrow \mathbb{R}^2$

$$\begin{pmatrix} E \\ p \end{pmatrix} = F \begin{pmatrix} \mathfrak{E} \\ \mathfrak{p} \end{pmatrix}, \tag{2}$$

which reduces to the identity for small energies

$$F \begin{pmatrix} E \ll M_{\text{Planck}} c^2 \\ p \ll M_{\text{Planck}} c \end{pmatrix} = \begin{pmatrix} E \\ p \end{pmatrix}. \tag{3}$$

Note that the group structure of the deformed transformations in Eq. (1) is the same as that of the ordinary

---

[¶] This article was submitted by the authors in English.

Lorentz group. This appears quite reasonable as the only suitable six-parameter extension (cf. [6, 7, 18]) of the group $SO(3)$ of spatial rotations, which we want to retain, seems to be the Lorentz group itself, especially since we want to reproduce the usual Lorentz transformations at small energies. It should also be mentioned here that this approach relies on the particle picture—there is no unique and well-defined field-theoretic formulation at this stage.

2. Field-theoretic example. Unfortunately, there has so far been no unique prescription for translating the behavior in momentum space (E, p) into position space (t, x), which is required for formulating a corresponding field theory. There is not even consistency in the literature regarding the velocity of propagation of Planckian particles: in [19], it is argued that the speed of light does not depend on the energy (i.e., that all massless particles have the same velocity c) in all DSR theories. Work [20], on the other hand, arrives at the (natural) result that the propagation speed is given by the group velocity $v_g = dE/dp$. In [6], however, the phase velocity $v_p = E/p$ is used instead (in some limit). This depends on whether (and how) one modifies the commutators such as $[x, p] = i\hbar$ and, hence, the identifications $ip \longleftrightarrow \hbar\partial/\partial x$, etc., or not (see, e.g., [21, 22]).

However, let us consider one possible example for a field-theoretic formulation motivated by an analogy to condensed matter systems. The propagation of sound waves is governed by a dispersion relation, which is linear at low energies and shows deviations (sub- or supersonic) at high energies (cf. also [23–25]). Although there certainly exists a preferred frame in such systems, one might (formally) perform the same steps as described in the previous section and parameterize the nonlinear dispersion relation $E(p)$ with a nonunique function F as in Eq. (2) by $\mathfrak{E}^2 = c^2\mathfrak{p}^2$ (although here c denotes the speed of sound). In this somewhat artificial way, the usual linear Lorentz transformation $\mathscr{L}$ in the $(\mathfrak{E}, \mathfrak{p})$-space can be used to define transformations from one frame to another. In order to conduct a Lorentz transform of the field $\phi(t, x)$ (e.g., a wave packet), one first does a Fourier transform $\mathscr{F}$ assuming $ip \longleftrightarrow \hbar\partial/\partial x$, etc., then applies the nonlinear Lorentz transformation, and finally transforms back:

$$\phi(t, x) \longrightarrow \tilde{\phi}(E, p) = \mathscr{F}\phi,$$

$$\tilde{\phi}(E, p) \longrightarrow \tilde{\phi}(E', p'), \qquad (4)$$

$$\phi'(t, x) = \mathscr{F}^\dagger\tilde{\phi}(E', p').$$

Since the function F and its inverse F^{-1}, as well as the dispersion relation $E(p)$, are nonpolynomial in general, the above procedure is clearly nonlocal in position space (t, x) (see also Sections 4 and 5 below).

3. Energy of composite systems. As mentioned in the Introduction, one of the main motivations for deforming the usual Lorentz boosts is to require that not only the speed of light (at low energies) but also the

Planck scale is invariant[1] under the modified transformations, hence the notion "doubly special relativity". Since the usual linear Lorentz boosts $\mathscr{L}$ do not possess any fixed points (in E, p) except zero and infinity, and Eq. (3) connects $E = p = 0$ to $\mathfrak{E} = \mathfrak{p} = 0$, the Planck scale must be mapped by the function F^{-1} to infinity in order to be invariant. As we shall see below, this property has rather dramatic consequences for composite systems.

Demanding that energy-momentum conservation in one frame has to be equivalent to energy-momentum conservation in all frames implies the following nonlinear composition law[2]

$$\begin{pmatrix} E_{\text{total}} \\ p_{\text{total}} \end{pmatrix} = F_{(N)}\left[\sum_{i=1}^{N} F^{-1}\begin{pmatrix} E_i \\ p_i \end{pmatrix}\right], \qquad (5)$$

i.e., one has to add $\mathfrak{E}_i$ and $\mathfrak{p}_i$ (see, e.g., [7, 18]). The subscript (N) indicates that the function $F_{(N)}$ could be modified, i.e., differ from F.

Let us first discuss the implications of using the same [18] function as in the one-particle case $F_{(N)} = F$: since F maps infinity to the Planck scale, the total energy can never exceed the Planck energy, which is a weird result and raises serious questions concerning the physical significance of such an energy concept (see, e.g., [7]). Moreover, a Galilei-type argument points out another contradiction if the velocity of propagation depends on energy (see also the next section): if two or more particles have equal energies E and, hence, velocities v, then the speed of the composite system obviously should be the same. However, according to Eq. (5) with $F_{(N)} = F$, the total energy E_{total} of the composite system is closer to the limiting Planck energy and, hence, the derived velocity would be different!

Alternatively, it has been suggested [7] that one constructs $F_{(N)}$ by replacing M_{Planck} with NM_{Planck} in the explicit expression for F. In that case, one has to know how many elementary particles the system is composed of, which seems to be rather artificial (see, e.g., [18]). For example, in addition to the arguments presented in [18], if merely one particle has the Planck energy (or very nearly so), adding one photon with an arbitrarily small energy to the system increases the total energy by $M_{\text{Planck}}c^2$, which is also an odd feature of this construction.

In view of the above considerations, one might question the physical significance of the quantities E and p in comparison with $\mathfrak{E}$ and $\mathfrak{p}$. The laws of energy-momentum conservation assume a much simpler form in terms of $\mathfrak{E}$ and $\mathfrak{p}$ [26]. Apparently, the only justifica-

---

[1] In this sense, the idea of DSR can be compared to the transition from the Galilei transformations (no invariant velocity) to special relativity (cf. [1, 2]).

[2] The main argument is basically the same as for the usual linear Lorentz transformations where (under certain assumptions, such as commutativity) only a linear composition law is invariant (see, e.g., [18]).

tion for considering E and p instead of $\mathfrak{E}$ and $\mathfrak{p}$ could be that the former quantities, E and p, are related to the spacetime behavior and determine the energy-dependent velocity of propagation, etc., whereas the latter, $\mathfrak{E}$ and $\mathfrak{p}$, are not.

4. Energy-dependent speed of light. Since the dispersion relation $E(p)$ must assume the same form in all frames, it can be derived from the usual invariant $\mathfrak{E}^2 = c^2\mathfrak{p}^2$ (remember $m = 0$) of the linear Lorentz transformations $\mathscr{L}$. Owing to the nonlinear function F, the dispersion relation can involve a rather complicated dependence $E(p)$ with a possibly changing speed of light (cf. the VSL cosmologies). As indicated above, a varying velocity of propagation seems to be the only possible way for the quantities E and p to acquire more physical significance than $\mathfrak{E}$ and $\mathfrak{p}$.

Obviously, the particle picture, which the whole approach is based on, and the concept of a velocity of propagation derived therefrom do only make sense if we are able to localize the particle under consideration with a (space/time) uncertainty much smaller than the length of the particle's world line. For example, we may derive the velocity of a Planckian particle by determining its position within a few Planck lengths and following its propagation over a macroscopic time duration and distance. Here, macroscopic means much larger than the Planck length/time (we want to retain the usual spacetime translation symmetry and the concept of internal motion).

As motivated in the previous section, the inverse function F^{-1} diverges at the Planck scale and, hence, cannot be written as a polynomial (polynomials are regular everywhere). In general, one would expect $E(p)$ to be singular at the Planck scale as well, also displaying a nonpolynomial behavior, and, therefore, nonlocal effects to arise. At a first glance, one might argue that these nonlocalities occur in the Planck regime only and are, therefore, not problematic. However, as we shall now demonstrate, these nonlocal effects arise on a *macroscopic* scale, provided that the particles under consideration can travel a distance much larger than the Planck length (see the arguments above).

Let us consider the two limiting cases: for higher and higher energies, the speed of light goes to zero (subluminal dispersion) or to infinity (superluminal). In the first case, the particle basically stops moving and just sits there. Now, if we can localize this highly Planckian particle within a few Planck lengths for a finite time duration (i.e., much longer than the Planck time), this clearly singles out a preferred frame, since we are supposed to know how Lorentz boosts act on macroscopic (i.e., sub-Planckian) scales!

In order to further study this apparent contradiction, let us consider a concrete example. Here, one encounters a problem, since, as mentioned in Section 2, the velocity of propagation is not uniquely determined. In the following, we assume that the speed of the particle

is given by the group velocity dE/dp (cf. Section 2 and [20]) and choose a dispersion relation which is linear in some interval $p \in [p_1, p_2]$, though not with the usual proportionality factor c, say,

$$F\begin{pmatrix} E \\ p_1 \leq p \leq p_1 \end{pmatrix} = \begin{pmatrix} E/2 \\ p \end{pmatrix}. \qquad (6)$$

If we assume a very small boost velocity $v \ll c$ (Galilei limit), the Lorentz transformation in Eq. (1) acts as

$$\begin{pmatrix} E \\ p \end{pmatrix} \longrightarrow \begin{pmatrix} E' \\ p' \end{pmatrix} = \begin{pmatrix} E + vp/2 \\ p + 2vE/c^2 \end{pmatrix}$$
$$= \begin{pmatrix} 1 & v/2 \\ 2v/c^2 & 1 \end{pmatrix}\begin{pmatrix} E \\ p \end{pmatrix}, \qquad (7)$$

i.e., with v and c being replaced by $v/2$ and $c/2$.

Since the dispersion relation $E^2 = c^2p^2/4$ arising from Eq. (6) is linear (between p_1 and p_2), the Lorentz transformation in position space (t, x) ought to be the same as in momentum space (E, p)—no matter whether we consider a particle with $p_1 \leq p \leq p_2$ or a wave packet (cf. Section 2) with support in the interval $[p_2, p_3]$. In this way, the presence of the Planckian particle with $p_1 \leq p \leq p_2$ traveling over a long distance enforces a Lorentz boost with $v/2$ and $c/2$ instead of v and c—at macroscopic (sub-Planckian) scales!

Evidently, the same phenomenon occurs for a superluminal (speed of light goes to infinity) dispersion relation. Any Planckian particle with a sub- or superluminal velocity of propagation either introduces a preferred frame or necessitates the modification of the Lorentz transformation on its travel time and distance, i.e., on macroscopic (sub-Planckian) scales, which demonstrates the occurrence of large-scale nonlocality [27].

5. Loss of coincidence. The fact that the presence of a Planckian particle affects the Lorentz transformations has further bizarre consequences. If we go to $3 + 1$ dimensions, the position-space representation of the deformed Lorentz transformation described in Eq. (4) of Section 2 acts as

$$\phi'(t, \mathbf{r}) = \int dE' d^3p' dt' d^3r' \phi(t', \mathbf{r}')$$
$$\times \frac{1}{(2\pi)^4} e^{i[tE' - \mathbf{r}\cdot\mathbf{p}' - t'E(E', \mathbf{p}') + \mathbf{r}'\cdot\mathbf{p}(E', \mathbf{p}')]} \qquad (8)$$
$$= \int dt' d^3r' \, \mathfrak{E}(t, t', \mathbf{r}, \mathbf{r}')\phi(t', \mathbf{r}').$$

The nonlinearity in $E(E', \mathbf{p}')$ and $\mathbf{p}(E', \mathbf{p}')$ results in a very strange behavior under spacetime translations. For the sake of illustration, we again (as in the previous sec-

tion) consider a function F, which is linear both for low momenta and in some interval $p \in [p_1, p_2]$

$$F\begin{pmatrix} E \\ \mathbf{p} \end{pmatrix} = \begin{pmatrix} \begin{cases} E & : \mathbf{p}^2 \ll p_1^2 \\ E/2 & : p_1^2 > \mathbf{p}^2 > p_2^2 \end{cases} \\ \mathbf{p} \end{pmatrix}. \qquad (9)$$

Now, let us follow the evolution of two wave packets: one $\phi'_{\text{low}}(t, \mathbf{r})$ is decomposed of sub-Planckian energies $\mathbf{p}^2 \ll p_1^2$ and the other one $\phi'_{\text{Planck}}(t, \mathbf{r})$ contains momenta in the interval $p \in [p_1, p_2]$ only. In this situation, the transformation in Eq. (8) can be calculated easily, and in the Galilei limit $v \ll c$, we obtain (cf. Eq. (7))

$$\phi'_{\text{low}}(t, \mathbf{r}) = \phi_{\text{low}}(t' + \mathbf{r}' \cdot \mathbf{v}/c^2, \mathbf{r}' + \mathbf{v}t'),$$
$$\phi'_{\text{Planck}}(t, \mathbf{r}) = \phi_{\text{Planck}}(t' + 2\mathbf{r}' \cdot \mathbf{v}/c^2, \mathbf{r}' + \mathbf{v}t'/2). \qquad (10)$$

Note that the relativistic corrections to the time coordinates in the first arguments on the right-hand side are different due to the nonlinearity. Consequently, if we change the origin of our spatial coordinate system, we introduce a relative time shift

$$\mathbf{r}' \longrightarrow \mathbf{r}' + \mathbf{a} \rightsquigarrow \Delta t = \mathbf{a} \cdot \mathbf{v}/c^2, \qquad (11)$$

between the two wave packets. Ergo, if the velocities of the two wave packets and the boost direction v are linearly independent and the two wave packets hit each other (i.e., coincide within their width at some space-time region) in one coordinate system, they may miss each other (one wave packet comes too late) in another coordinate representation!

Of course, this breaking of translational (i.e., Poincaré) invariance, again on large scales, has been demonstrated using the special field-theoretic representation described in Section 2; and one could argue that the above effect is an artifact of the special construction in Section 2 and that in a different representation, this problem can be avoided. However, in order to prove this assertion, one has to provide another explicit field-theoretic example and to study its consequences. It seems that one faces similar difficulties, breaking of translational invariance $x_\mu \longrightarrow x_\mu + a_\mu$ (see, e.g., [28]) and deviations from the usual behavior on large scales $x_\mu \gg L_{\text{Planck}}$, when introducing noncommuting coordinates via

$$[x^\mu, x^\nu] = \Lambda^{\mu\nu\rho} x_\rho \qquad (12)$$

(instead of $[x^\mu, x^\nu] = \zeta g^{\mu\nu}$, for instance), as it is done, for example, in [21, 22] in relation to DSR theories.

We would also like to stress that the counterargument presented in the previous section is independent of any field-theoretic representation (and would, therefore, not go away).

6. Summary. Apart from the weird properties of composite systems discussed in Section 3, the theory of "doubly special relativity" goes along with violations of locality and separability if the speed of light depends on energy, since the presence of a single Planckian particle can modify the action of the Lorentz transformation at macroscopic scales[3] (i.e., much larger than the Planck length; see Sections 4 and 5). On the other hand, if the speed of light does not depend on the energy (e.g., the dispersion relation is $E^2 = c^2 p^2$), then there is no discernible reason to assign E more physical significance than $\mathfrak{E}$ (see Section 3). Although one should bear in mind that the whole approach purely relies on the particle picture (not a field theory), one would expect that the energy, defined as the generator of the time-translation symmetry, is an additive quantity for independent systems (which brings us back to the question of locality and separability).

In search of alternatives, one could imagine that, even though the (still to be found) underlying theory (including quantum gravity) might not possess a preferred frame, the physical state of the system describing the actual gravitational field, etc., indeed does introduce an effectively preferred frame with respect to the interaction with Planck-scale photons, for example, that propagate within the gravitational field.

After finishing the work on our manuscript, we found that several other authors (based on different approaches and assumptions) have also pointed out strange consequences of DSR and/or concluded that DSR is either inconsistent with our present understanding of physics or trivial (i.e., indistinguishable from ordinary special relativity; see [29–32]).

REFERENCES

1. G. Amelino-Camelia, Int. J. Mod. Phys. D **11**, 35 (2002); gr-qc/0012051.

2. G. Amelino-Camelia, Phys. Lett. B **510**, 255 (2001); hep-th/0012238.

---

[3] Note, however, that this result does not prove that DSR is conceptually inconsistent or in conflict with experiments or observations since we have not observed Planckian particles (at least not knowingly).

3. N. R. Bruno, G. Amelino-Camelia, and J. Kowalski-Glikman, Phys. Lett. B **522**, 133 (2001); hep-th/0107039.

4. G. Amelino-Camelia, Nature **418**, 34 (2002); gr-qc/0207049.

5. G. Amelino-Camelia, Int. J. Mod. Phys. D **11**, 1643 (2002); gr-qc/0210063.

6. J. Magueijo and L. Smolin, Phys. Rev. Lett. **88**, 190403 (2002); hep-th/0112090.

7. J. Magueijo and L. Smolin, Phys. Rev. D **67**, 044017 (2003); gr-qc/0207085.

8. G. Amelino-Camelia and T. Piran, Phys. Lett. B **497**, 265 (2001); hep-ph/0006210.

9. G. Amelino-Camelia and T. Piran, Phys. Rev. D **64**, 036005 (2001); astro-ph/0008107.

10. G. Amelino-Camelia, J. Lukierski, and A. Nowicki, Czech. J. Phys. **51**, 1247 (2001); hep-th/0103227.

11. K. Greisen, Phys. Rev. Lett. **16**, 748 (1966).

12. G. T. Zatsepin and V. A. Kuzmin, Pis'ma Zh. Éksp. Teor. Fiz. **4**, 114 (1966) [JETP Lett. **4**, 78 (1966)].

13. J. W. Moffat, Int. J. Mod. Phys. D **2**, 351 (1993); gr-qc/9211020.

14. M. A. Clayton and J. W. Moffat, Phys. Lett. B **460**, 263 (1999); gr-qc/9211020.

15. T. Jacobson, S. Liberati, and D. Mattingly, Phys. Rev. D **67**, 124011 (2003); hep-ph/0209264.

16. D. Mattingly, T. Jacobson, and S. Liberati, Phys. Rev. D **67**, 124012 (2003); hep-ph/0211466.

17. V. A. Kostelecky and R. Lehnert, Phys. Rev. D **63**, 065008 (2001); hep-th/0012060.

18. S. Judes and M. Visser, Phys. Rev. D **68**, 045001 (2003); gr-qc/0205067.

19. M. Daszkiewicz, K. Imilkowska, and J. Kowalski-Glikman, hep-th/0304027.

20. G. Amelino-Camelia, F. D'Andrea, and G. Mandanici, hep-th/0211022.

21. J. Kowalski-Glikman and S. Nowak, Phys. Lett. B **539**, 126 (2002); hep-th/0203040.

22. J. Kowalski-Glikman and S. Nowak, Int. J. Mod. Phys. D **12**, 299 (2003); hep-th/0204245.

23. T. Jacobson, Phys. Rev. D **48**, 728 (1993); hep-th/9303103.

24. W. G. Unruh, Phys. Rev. D **51**, 2827 (1995); gr-qc/9409008.

25. S. Corley and T. Jacobson, Phys. Rev. D **54**, 1568 (1996); hep-th/9601073.

26. At least for $F_{(N)} = F$ or for $N_{\text{initial}} = N_{\text{final}}$. In these cases Eq. (5) implies $\sum_i \mathfrak{E}_i^{\text{initial}} = \sum_i \mathfrak{E}_i^{\text{final}}$ as well as $\sum_i \mathfrak{p}_i^{\text{initial}} = \sum_i \mathfrak{p}_i^{\text{final}}$. In view of this observation, it is hard to see how DSR can solve the threshold anomalies—such as the UHECR problem—which are basically based on energy conservation arguments, because one should be able to choose initial and final configurations with the same number of particles; and at low energies, we have $\mathfrak{E}_i = E_i$. (Unless, of course, one argues that the cross section changes significantly at high energies, for example due to an energy-dependent speed of light.)

27. Consider the following *gedanken* experiment: Let us assume that we can localize the (sub-luminal) Planckian photon with almost zero velocity within 1 cm for a few seconds. Now we build a box made of ordinary (sub-Planckian) material around the Planckian photon, which is nearly at rest. Another (inertial) observer, however, who walks by at 1 m/s, also sees the Planckian photon standing still (remember: no preferred frame). So either this observer sees the Planckian photon (eventually) outside the box or, even more drastically, the (sub-Planckian) box following him/her. In both cases, locality is violated. Imagine, for example, that the Planckian photon interacts with some ordinary matter inside the box; and, without non-locality, we know how ordinary matter and space–time behave on large scales.

28. O. Bertolami and L. Guisado, hep-th/0306176.

29. J. Lukierski and A. Nowicki, Int. J. Mod. Phys. A **18**, 7 (2003); hep-th/0203065.

30. J. Rembielinski and K. A. Smolinski, Bull. Soc. Sci. Lett. Lodz **53**, 57 (2003); hep-th/0207031.

31. D. V. Ahluwalia-Khalilova, gr-qc/0212128.

32. D. Grumiller, W. Kummer, and D. V. Vassilevich, Ukr. Phys. J. **48**, 329 (2003); hep-th/0301061.

Optical Conductivity of Single Walled Nanotube Films in the Terahertz Region[¶]

J. Han[1]*, Z. Zhu[1], Y. Liao[2], Z. Wang[1], L. Yu[1], W. Zhang[1], L. Sun[1], and T. Wang[1]

[1] *Shanghai Institute of Nuclear Research, Chinese Academy of Sciences, Shanghai, 201800 China*
[2] *Yunnan Astronomical Observatory, Chinese Academy of Sciences, Kunming 650011, China*
*e-mail: han@sinr.ac.cn
Received August 12, 2003

A theoretical investigation for the conductivity of single walled nanotube films is carried out with an effective medium model in the Terahertz region. The results are compared with the recent experiment and a decrease of the real conductivity with increasing frequency is predicted. Meanwhile, the off-diagonal components of the dielectric function of single-walled carbon nanotube films based on the magnetooptical effects are also shown. © 2003 MAIK "Nauka/Interperiodica".

PACS numbers: 78.67.Ch; 78.66.-w; 78.20.Ls

Recently, terahertz (THz) technology is becoming a very attractive research field because its applications have involved semiconductor, label-free genetic analysis, cellular-level imaging, biological sensing, and so on [1]. Its applications in nanotubes appear to be opening up a new field, since the nanotubes have been recognized as a fascinating material for their many unique properties. Studies of T-ray interaction with nanotubes will explore the potential application of T-ray in nanostructures. It is possible to measure both the diagonal and off-diagonal components of the complex conductivity tensor due to the current advances in THz spectroscopy [2, 3]. The electronic and optical properties of nanotubes in low frequency have been reported by some works [4–7] so far, but few studies are performed in the THz region. In this paper, we report on a theoretical analysis of the conductivities of the single-walled carbon nanotube films in the THz region from 0.1 to 10 THz.

In the recent experiment, Jeon and his collaborators [7] measured the absorption and index of refraction of the SWNT films using an optoelectronic THz beam system from 0.1 to 0.8 THz. The conductivity of the film is thereby learned. The experiment indicates that the real conductivity increases with increasing frequency. The previous investigations have done some research about the far-infrared characteristic of SWNT films [8–10]; however, the results are not consistent when considering the overlapping frequency region.

As we know, the optical properties of metal and semiconductors usually satisfy the simple Drude theory. However, the SWNT film cannot be interpreted within a simple Drude model because of its special characters. In this work, we employ the effectivity

medium approximation (EMA) method, which is also known as the Maxwell–Garnett (MG) model [11, 12], to interpret the experimental results. The EMA is denoted as the following:

$$\varepsilon(\omega) = \varepsilon_i \frac{2(1-f)\varepsilon_i + (1+2f)\varepsilon_m(\omega)}{(2+f)\varepsilon_i + (1-f)\varepsilon_m(\omega)}, \quad (1)$$

where the filling factor f defines the volume fraction of the insulator; ε_i and $\varepsilon_m(\omega)$ are the host-medium dielectric function and the metal dielectric function, respectively. Usually, the EMA is used to describe the dielectric constant of the structures that metal particles are in a continuous insulating matrix of and the insulators for a continuous medium. Here, the SWNT films are considered as CNTs embedded in an effective dielectric medium. In our calculation, $f = 0.6$ is given, and ε_i and $\varepsilon_m(\omega)$ can be determined from the Drude–Lorentzian (DL) model. From the DL model, the dielectric function is given by

$$\varepsilon(\omega) = \varepsilon_c - \frac{\omega_p^2}{\omega(\omega + i\Gamma)} - \sum_j \frac{\omega_{pj}^2}{(\omega^2 - \omega_j^2) + i\Gamma_j\omega}, \quad (2)$$

where ε_c represents the frequency-independent optical dielectric constant. The second term is a Drude term which defines the delocalized charge component; ω_p and Γ are the plasma frequency and the relaxation rate of the charge carries, respectively [10, 13]. The motion of localized charge carriers is ascribed to the third term, the Lorentz harmonic oscillators, where ω_{pj}, ω_j, and Γ_j are the center frequency, spectral width, and oscillator strength, respectively. The metallic particles $\varepsilon_m(\omega)$ can be defined by the Drude term, the host-medium ε_i can be represented by a Lorentz term adding ε_c with the relevant parameters. Parameters for the model calculation

---

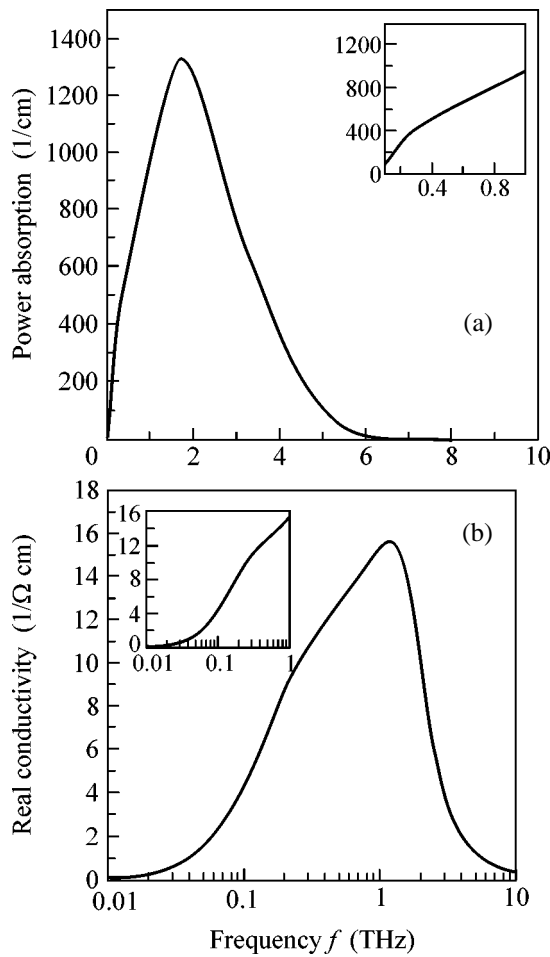[¶] This article was submitted by the authors in English.

Fig. 1. The power absorption [$\alpha(\omega)$] (a) and the real parts of the conductivity [$\sigma_1(\omega)$] (b) of SWNT film are obtained by a Kramers–Kronig analysis of the dielectric function. The insets are below 1.0 THz.

Fig. 2. The real part of optical conductivities [$\sigma_1(\omega)$] calculated with different filling factor f.

a pair of integers (n, m). Hamada *et al.* [15] pointed out that armchair SWNTs of $n = m$ are gapless and should be metallic, while zigzag or chiral SWNTs of $n \neq m$ have a gap depending on the wrapping vector. These gaps could be reasonable for the features of nanotubes. In our calculations, the sample of the single walled nanotube film is a composite consisting of a random mixture of tubes of different types, oriented rather randomly at least within the plane of the film. Moreover, we have performed an MG calculation with different filling factors f, shown in Fig. 2, which assumed a different constituent of nanotube films, and found that a peak still appeared. Therefore, we conclude that the gap is essential to the sample constituent and also gives rise to the optical conductivity peak at 1.0 THz [9].

We remark that, although the purified and pristine samples, and also different orientations are measured in Jeon's experiment [7], our interest is in the purified sample. We find that the conductivity has the same tendency for different orientations. The optical conductivity curves calculated for several filling factors f are given in Fig. 2. The different f stands for the volume fraction and shapes of metallic tubes with ε_m, and in some degree we also consider that it reflects the effect of orientations. In Fig. 2, the results of calculations closely resemble the measurement conductivity as f between 0.3 and 0.8. When the frequency is above 4.0 THz, the real part of the conductivity is essentially frequency-independent. This indicates a Drude conductivity with a pronounced scattering rate above 4.0 THz.

The measurements of optical reflection can be used to determine the diagonal elements of the dielectric tensor. However, it is not permitted to obtain the off-diagonal components. Therefore, another method based on the magnetooptical Kerr effect technique could be used [2]. The magnetooptical properties of the films will

are defined by $\varepsilon_c = 5.5$, $\omega_p = 0.03$ eV, $\omega_{pj} = 0.02$ eV, $\Gamma = 0.0035$ eV, $\omega_j = 0.004$ eV, and $\Gamma_j = 0.02$ eV, which based on the analysis of Jeon's experiment. A filling factor $f = 0.6$ is considered [14].

The best fits for Jeon's experiment are presented in Fig. 1. The dielectric function is calculated by the MG approach, the power absorption and the real part of the conductivity of SWNT films are obtained through a Kramers–Kronig (KK) transformation. In the insets of Fig. 1, as shown, the absorption and the conductivity increase with increasing frequency within 0.1 to 1.0 THz, which agrees with the experimental results. The conductivity displays a strong peak at about 1.0 THz, corresponding to a localized absorption. When the frequency is greater than 1.0 THz, the fitting curve gives a decrease with increasing frequency, which is not represented in Jeon's experiment due to the limit of the device. However, this decline has been reported by the experiments [7, 11]. In general, the electronic structure of individual SWNT is specified by
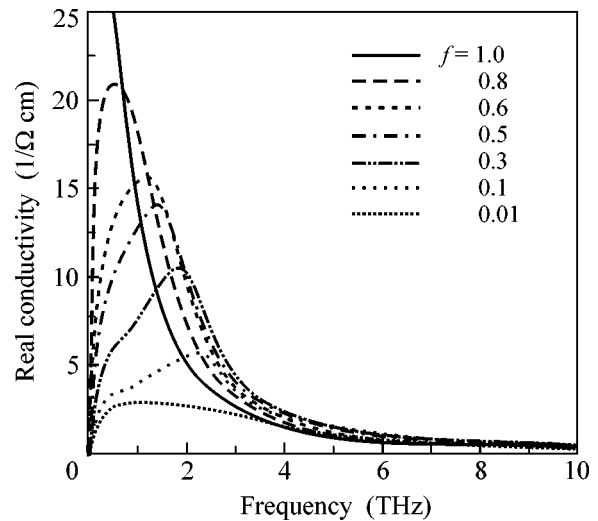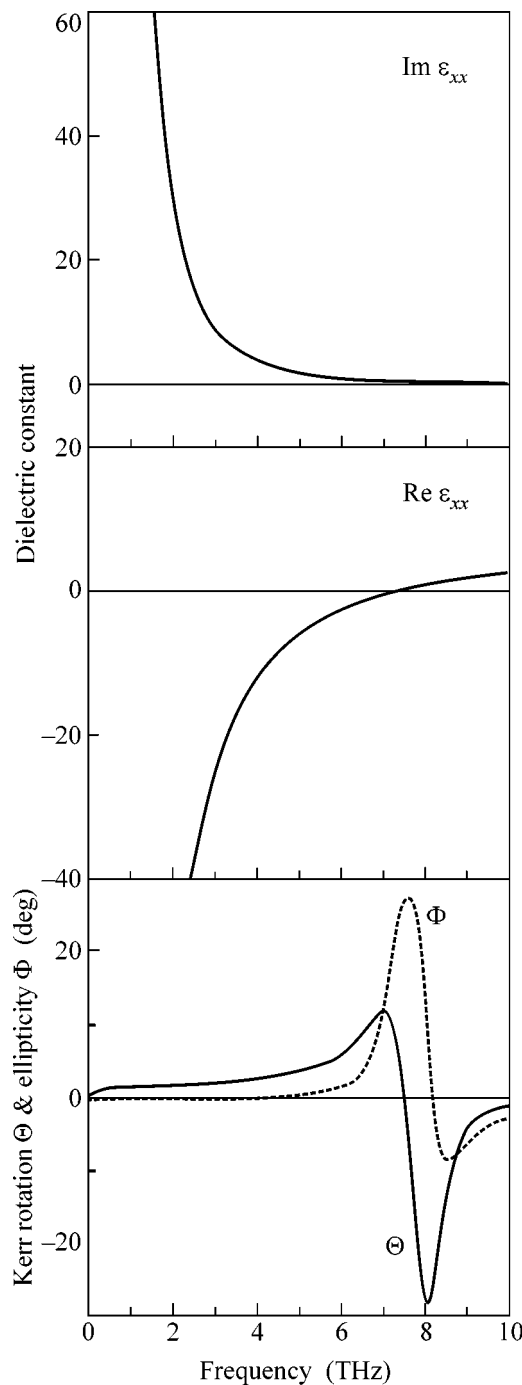
Fig. 3. Dielectric constant and Kerr effect rotation and ellipticity calculated by the Drude model with the fitting parameters based on Jeon's experiment.

offer more information about the off-diagonal components when a static magnetic field is perpendicular to the sample surface.

In order to find the change of the optical conductivity of the SWNT films when they are in an external magnetic field **B**, we present our model calculation with the Drude theory [2, 17]. In a Cartesian coordinate frame, taking the *z* axis as normal to the sample surface and considering **B** parallel to the *z* direction, the nonzero elements of the dielectric tensor in the Drude model are given by the formulas

$$\varepsilon_{xx} = \varepsilon_{yy} = \varepsilon_c\left[1 - \frac{\omega_p^2(\omega^2 + i\Gamma\omega)}{(\omega^2 + i\Gamma\omega)^2 - \omega^2\omega_c^2}\right], \quad (3)$$

$$\varepsilon_{xy} = -\varepsilon_{yx} = \frac{i\varepsilon_c\omega_p^2\omega\omega_c}{(\omega^2 + i\Gamma\omega)^2 - \omega^2\omega_c^2}, \quad (4)$$

$$\varepsilon_{zz} = \varepsilon_c\left[1 - \frac{\omega_p^2}{(\omega^2 + i\Gamma\omega)}\right], \quad (5)$$

where $\omega_c = eB/m^*$ is the cyclotron frequency, which can be determined from measurements of the absorption or reflection of circularly polarized electromagnetic waves with frequency ω. The absorption or reflection increase strongly when $\omega = \omega_c$. In our calculations, $\omega_c = 0.0018$ eV is taken when supposing the magnetic field of $B = 0.5$ T. The off-diagonal part of the dielectric tensor ε_{xy}, which arises from interband and intraband transition, is reasonable for the magnetooptical effects [16]. The Kerr rotation ϕ and ellipticity φ can be calculated from [17, 18]: $\theta + i\phi = \varepsilon_{xy}/[\sqrt{\varepsilon_{xx}}(1 - \varepsilon_{xx})]$. In Fig. 3, the curves show the real, imaginary part of the diagonal elements of the dielectric function, the Kerr rotation, and ellipticity with the aforementioned parameters. From Fig. 3, we found that at the plasma resonance $\omega_p = 7.26$ THz ε_{xx} disappears, and ε_{xx} is equal to 1.0 at 8.0 THz. In this region, the signals of the magnetooptical Kerr effect are enhanced. The dispersion in the diagonal part of the dielectric tensor and the influence of the plasma resonance may induce the strength of the magnetooptical Kerr effect. This phenomenon has also been investigated in some other metallic materials [17]. The off-diagonal elements of the conductivity tensor are crucial to the material Hall effect and transport properties in our investigation. The magnetooptical measurement technique, especially in the THz region, and an effective theoretical interpretation are a useful resource for studying the unknown properties of nanotubes.

In summary, we have theoretically interpreted the optical characteristic of SWNT films based on Jeon's experiment, and predicted that the conductivity of the similar sample will decrease with increasing frequency when the frequency is above 1.0 THz. Moreover, we discussed the dielectric function of single-walled nanotube films in an external magnetic field and found that it exhibits a pronounced magnetooptical Kerr effect. The results display a resonant enhancement of Kerr rotation and ellipticity due to magnetoplasma resonance in the films. It is also shown that the combination of Maxwell–Garnett and Drude–Lorentz model is an effective medium approach, and that it can describe

more remarkable results in the THz region for the research of optical properties of materials.

REFERENCES

1. Bradley Ferguson and Xi-Cheng Zhang, Nat. Mater. **1**, 26 (2002).

2. R. Shimano, Y. Ino, Yu. P. Svirko, and M. Kuwata-Gonokami, Appl. Phys. Lett. **81**, 199 (2002).

3. Takeshi Nagashima and Masanori Hangyo, Appl. Phys. Lett. **79**, 3917 (2001).

4. Y.-P. Zhao, B. Q. Wei, P. M. Ajayan, *et al.*, Phys. Rev. B **64**, 201402 (2001).

5. C. Phillips, M. Y. Su, J. Ko, *et al.*, Physica E (Amsterdam) **7**, 814 (2000).

6. Y.-C. Chen *et al.*, Appl. Phys. Lett. **81**, 1 (2002).

7. Tae-In Jeon, Keun-Ju Kin, Chul Kang, *et al.*, Appl. Phys. Lett. **80**, 3403 (2002).

8. B. Ruzicka, L. Degiorgi, R. Gaal, *et al.*, Phys. Rev. B **61**, R2468 (2000).

9. A. Ugawa, A. G. Rinzler, and D. B. Tanner, Phys. Rev. B **60**, R11305 (1999).

10. O. Hilt, H. B. Brom, and M. Ahlskog, Phys. Rev. B **61**, R5129 (2000).

11. F. Bommeli, L. Degiorgi, P. Wachter, *et al.*, Solid State Commun. **99**, 513 (1996).

12. R. W. Cohen, G. D. Cody, M. D. Coutts, and B. Abeles, Phys. Rev. B **8**, 3689 (1973).

13. T. Pichler, M. Knupfer, M. S. Golden, *et al.*, Phys. Rev. Lett. **80**, 4729 (1998).

14. E. A. Taft and H. R. Philipp, Phys. Rev. A **138**, 197 (1965).

15. N. Hamada, S. Sawada, and A. Oshiyama, Phys. Rev. Lett. **68**, 1579 (1992).

16. D. Dragoman and M. Dragoman, *Optical Characterization of Solid* (Springer, Berlin, 2002).

17. H. Feil and C. Hass, Phys. Rev. Lett. **58**, 65 (1987).

18. P. N. Argyres, Phys. Rev. **97**, 334 (1955).

Novel Superconducting Niobium Beryllide Nb₃Be with A15 Structure

A. Zh. Tuleushev*, V. N. Volodin, and Yu. Zh. Tuleushev

National Nuclear Center, Institute of Nuclear Physics, 480082 Almaty, Kazakhstan
*e-mail: tuleushev@inp.kz
Received August 20, 2003

New niobium beryllide Nb_3Be with A15 structure and lattice parameter $a = 0.5187 \pm 0.0007$ nm, coexisting (3–5%) with a tetragonal phase, presumably, of an ordered solid solution with parameters $a = 0.5414 \pm 0.0008$ nm and $c = 0.6378 \pm 0.0009$ nm, was synthesized by thermal treatment (875–1100°C) of amorphous film coatings containing 26.8–32.4 at. % Be and formed from short-period Nb and Be layers by magnetron sputtering. The domain of existence of the Nb_3Be phase and the critical superconducting transition temperature (10.0 K and a transition width of 2.5 K) were determined and the X-ray structural data for structure identification were obtained. © 2003 MAIK "Nauka/Interperiodica".

PACS numbers: 74.78.Db; 74.70.Ad

It was established in [1, 2] that film systems prepared from short-period Nb–Sn, Nb–Al, and Nb–Pb layers by the magnetron technique include α-Nb-based solid solutions, in which the concentrations of the second metal corresponded to the domain of existence of intermetallic phases. In turn, the obtained compositions served as starting materials for the diffusionless synthesis of intermetallic superconducting films with the A15 lattice at temperatures appreciably lower than the temperatures used in other methods. The lattice parameters a found for Nb_3Sn and Nb_3Al intermetallides prepared by the above-mentioned method were in compliance with the tabulated data, and their superconducting characteristics were confirmed [1].

The lattice parameters determined for the Nb_3Pb intermetallide [2] were different from the literature data. In [3], this intermetallide was assigned the value $a = 0.5256$ nm, and the critical superconducting transition temperature T_c varied from 1.2 K [4] to 9.6 K [5]. To our knowledge, works devoted to the simultaneous determination of the structure and critical properties of this intermetallide are now lacking. Cryogenic studies of the Nb_3Pb film with structure A15 and $a = 0.5952$ nm, synthesized by us in [2], showed that $T_c = 5.6$ K and the transition width was 0.2 K (see below).

It follows from the comparison of the T_c values known for a number of niobium p^2-metal intermetallides with lattice parameters a that a and T_c are related to each other by a simple power law. Our measurement of the parameters of the superconducting Nb_3Pb intermetallide confirms the assumption made in [6] that the T_c temperature of the only as yet unsynthesized pure Nb_3Si intermetallide of this series with A15 lattice and expected lattice parameter $a = 0.5210$ nm can be as high

as 25 K. In turn, the lattice parameter of these intermetallides is determined by the atomic size of the second metal; namely, T_c increases with a decrease in this size. In this respect, of interest was to synthesize niobium-based A15 intermetallides with light metals having small atomic sizes. Since the Be atoms have the smallest size (0.1246 nm), we undertook a successful attempt to synthesize niobium beryllide of the formula Nb_3Be, determined its structure and critical temperature T_c, and obtained the data for compound identification.

The Nb–Be system is known to include five intermetallic compounds: Nb_3Be_2, $NbBe_2$, $NbBe_3$, Nb_2Be_{17}, and $NbBe_{12}$. The Nb_3Be_2, $NbBe_3$, and Nb_2Be_{17} compounds melt congruently at >1700, >1650 ± 50, and 1800 ± 50°C, respectively. The $NbBe_2$ and $NbBe_{12}$ compounds are prepared through the peritectic reactions at 1630 ± 30 and 1672 ± 5°C, respectively. No compounds exist at Nb concentrations higher than 60 at. % [7].

In our experiments, Nb of 99.95 wt % purity and Be of 99.99 wt % purity were used. Films formed from the short-period nanosized layers of the components were deposited onto polycore (α-Al₂O₃) substrates at temperatures up to 150°C. The overall thickness of the layers in the films was 1000 nm. On assumption that the expected Nb_3Be intermetallide has a homogeneity region, samples with sub- and overstoichiometric compositions were prepared and used for the investigation in the Be concentration range 22.8–32.4 at. %. In the course of coating, the ratio of the deposited components was monitored by the weight method from the sputtered and deposited amount of each metal. The synthesis of Nb_3Be in the resulting coatings was initiated by heating at a pressure of $10^{-1}–10^{-2}$ Pa. Thermal treat-

ment of the primary compositions was accomplished by cyclic heating of the samples at temperatures from 500 to 1100°C with a step of 25°C and phase-state control after each annealing procedure. The X-ray structural studies were carried out on a diffractometer with cobalt radiation $\lambda_{k\alpha} = 0.179021$ nm and a graphite monochromator. The lattice parameters were calculated as averages over all diffraction reflections used for a given phase.

The coatings with beryllium contents of 22.8 and 23.8 at. % represented solid solutions with the α-Nb structure and $a = 0.3336 \pm 0.0004$ and 0.3345 ± 0.0002 nm, respectively. The coatings with 26.4, 28.8, 29.0, 29.1, and 32.4 at. % of Be were amorphous.

In accordance with the phase diagram [7], heating of the film samples of solid solutions to 600°C gave rise to the Nb_3Be_2 phase, which had the tabulated lattice parameter and coexisted with α-Nb ($a = 0.3311 \pm 0.0003$ nm) in the coating. Further thermal treatment of these samples did not reveal any changes in the film phase composition over the entire temperature range studied.

In the amorphous films with Be content ranging from 26.4 to 32.4 at. %, the amorphous phase converted at 500°C into a solid solution with the α-Nb structure and $a = 0.3280 \pm 0.0003$ nm. The rise in the annealing temperature to 650°C was accompanied by the isolation of a tetragonal phase with $a = 0.5414 \pm 0.0008$ nm, $c = 0.6378 \pm 0.0009$ nm, and an estimated content of 3–5%, whose presence was presumably due to a partial ordering of the solid solution. In addition to α-Nb ($a = 0.3292 \pm 0.0003$ nm) and the above-mentioned tetragonal phase with its parameters, a cubic phase with the A15 structure and $a = 0.5187 \pm 0.0007$ nm appeared at 875°C. After annealing at 950°C, the coating included only the A15 and tetragonal phases, with an unchanged amount and structure of the latter (Fig. 1). At a temperature of 1050°C, the A15 phase started to convert into α-niobium, and, after reaching 1100°C, the coatings were mixtures of α-niobium ($a = 0.3279 \pm 0.0004$ nm), the tetragonal phase (in an amount of 25–30%) with lattice parameters $a = 0.5376 \pm 0.0012$ nm $c = 0.6474 \pm 0.0011$ nm, and the traces of the A15 phase. The X-ray data for the identification of niobium beryllide Nb_3Be are given in the table.

The relative intensities given in the table do not fully conform the standard distribution because of the presence of film texture.

The cryogenic electrical-resistance four-probe tests of the sample annealed at 950°C with a starting Be content of 26.4 at. % showed that its critical superconducting transition temperature was 10.0 K and the transition width was 2.5 K (Fig. 2).

Taking into account that the Nb-to-Be ratio in the films was close to its stoichiometric value, that the lattice structure of the prepared intermetallide was of the A15 type, and that the coatings showed superconduct-
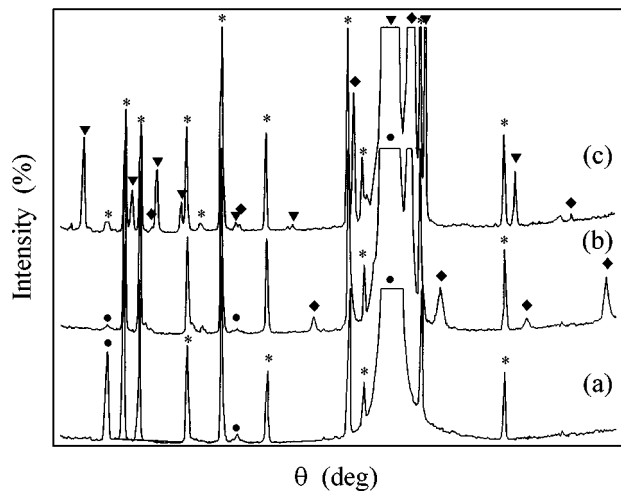
Fig. 1. Temperature-induced phase transformations in the Nb–Be sample with 29.13 at. % of Be: (a) 500, (b) 700, and (c) 950°C. (∗) Polycore; (●) solid solution of Be in Nb; (◆) tetragonal phase with $a = 5.414$ Å and $c = 6.378$ Å (ordered solid solution); and (▼) Nb_3Be phase with the A15 structure.

ing properties, we concluded that the synthesized phase corresponded to the Nb_3Be compound.

Evidently, such synthesis is possible only if the components are mixed at a temperature appreciably lower than the activation threshold for the formation of any phases in the system, as it occurred in our study. Then the question arises of the conditions for the applicability of phase diagrams obtained by the method of mixing initial components through melting (melting-type diagrams) to the prediction of phase distributions using low-temperature mixing of components by the magnetron technique.

In our opinion, when estimating the possibility of using melting-type phase diagrams as a basis of phase-equilibrium analysis of the systems obtained through

Interplanar spacing in the Nb_3Be phase

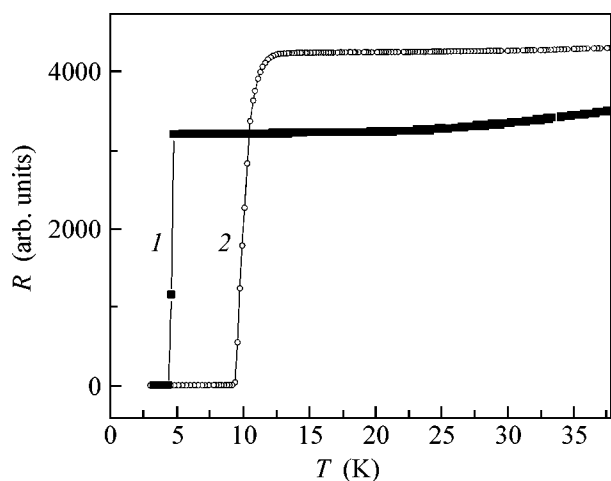| Angle, $\Theta°$	Interplanar distances d_{hkl}, nm	Plane indices (hkl)	Relative intensities I/I_0
14.12	0.3669	(110)	1.46
20.20	0.2592	(200)	7.28
22.70	0.2319	(210)	100
25.01	0.2117	(211)	3.62
29.24	0.1832	(220)	0.13
33.10	0.1639	(310)	0.21
36.70	0.1498	(222)	0.61
38.45	0.1439	(320)	1.54
40.20	0.1387	(321)	1.04
43.68	0.1296	(400)	2.31

Fig. 2. Temperature dependences of electrical resistances of the (*1*) Nb$_3$Pb and (*2*) Nb$_3$Be coating samples.

the low-temperature mixing of components, one should bear in mind that, in melting, the system components mix at temperatures higher than the activation threshold for the possible irreversible intermetallization reactions. The second Hume–Rothery rule, according to which the formation of stable intermediate compounds narrows the region of the primary solid solutions, leads to the same conclusion, although in different terms. It follows that, when using the low-temperature mixing technique followed by heating, the well-known melting-type phase diagrams can be supplemented by phases which cannot be formed by the melting-type mixing technology, as was demonstrated in this work.

Thus, new niobium beryllide Nb$_3$Be with the A15 structure has been synthesized by thermal treatment of the amorphous film system obtained by the magnetron technique from short-period Nb–Be layers in the Be concentration range 26.8–32.4 at. %; the temperature of existence was found to range from 875 to 1100°C; the critical superconducting transition temperature was determined (10.0 K); and the X-ray structural data for structure identification were obtained.

REFERENCES

1. A. Zh. Tuleushev, Yu. Zh. Tuleushev, and V. N. Volodin, Fiz. Met. Metalloved. **94** (4), 77 (2002).
2. A. Zh. Tuleushev, Yu. Zh. Tuleushev, and V. N. Volodin, Fiz. Met. Metalloved. **94** (5), 74 (2002).
3. H. Holleck, H. Nowotny, and F. Benesovsky, Monatsh. Chem. **94**, 2 (1963).
4. N. V. Ageev, N. E. Alekseevskiĭ, and V. F. Shamraĭ, *Crystalline Structure and Properties of Metallic Alloys* (Nauka, Moscow, 1978).
5. *Physical Quantities. Handbook*, Ed. by I. S. Grigor'ev and E. Z. Meĭlikhov (Énergoatomizdat, Moscow, 1991).
6. Hiroshi Iwasaki, Sci. Rep. Res. Inst. Tohoku Univ. A **31** (1) (1983).
7. *Phase Diagrams of Binary Metallic Systems: A Handbook*, Ed. by N. P. Lyakishev (Mashinostroenie, Moscow, 1996).

Translated by V. Sakun

Statistics of Eigenfunctions of Chaotic Billiards Taking Account of the Rashba Spin–Orbit Interaction

E. N. Bulgakov and A. F. Sadreev

Kirenskiĭ Institute of Physics, Siberian Division, Russian Academy of Sciences,
Akademgorodok, Krasnoyarsk, 660036 Russia
Received July 21, 2003; in final form, August 28, 2003

It is demonstrated, both analytically and numerically, that eigenfunction statistics in chaotic billiards with spin–orbit interaction fundamentally depend on the ratio of the squared spin–orbit interaction constant. If this ratio is small, one of the eigenstate components is a random Gaussian field, whereas another is not universal and depends on the billiard type. In the opposite case, the statistics of both components is described by the independent random complex Gaussian fields with the same variances. In the intermediate case, both eigenfunction components do not satisfy Gaussian statistics. © 2003 MAIK "Nauka/Interperiodica".

PACS numbers: 05.45.Mt; 73.21.La

In typical III–V semiconductor heterostructures, electrons form two-dimensional electron gas between layers [1, 2]. At helium temperatures, the coherence length is as high as several microns. By appropriately choosing the shape of surface electrode, one can confine electrons in an arbitrarily shaped quantum dot, which will be called a two-dimensional billiard. Such heterostructures are characterized by the Rashba spin–orbit interaction (SOI) [3], which modifies the Hamiltonian as

$$H = \frac{-\hbar^2}{2m^*}\nabla^2 + \hbar K[\sigma \times \mathbf{p})]_z, \qquad (1)$$

where m^* is the electron effective mass. The SOI constant K is proportional to the averaged interface electric field $\langle E \rangle = \langle -(1/e)(dE_c/dz) + E_i \rangle$, where E_c is the conduction band profile along the z axis perpendicular to the interface plane and E_i is the electric field between the donor impurities and two-dimensional electron gas [4]. Typically, one has for $\hbar^2 K = (1–10) \times 10^{-7}$ meV cm [5–7]. Apart from the Rashba SOI, there is an additional contribution caused by the inhomogeneous (confinement) potential that forms a billiard [8, 9]. However, if the confinement potential is approximated by hard walls, this contribution to the SOI can be ignored [9].

We use the billiard size R as the characteristic scale to rewrite Eq. (1) in the dimensionless form

$$\tilde{H} = \begin{pmatrix} -\nabla^2 & \beta\left(-\dfrac{\partial}{\partial x} + i\dfrac{\partial}{\partial y}\right) \\[2mm] \beta\left(\dfrac{\partial}{\partial x} + i\dfrac{\partial}{\partial y}\right) & -\nabla^2 \end{pmatrix}, \qquad (2)$$

where $\beta = 2m^*KR$ and all dimensionless coordinates are normalized to R. Then the Schrödinger equation for the spinor components takes the form

$$-\nabla^2\phi + \beta L\chi = \epsilon\phi,$$
$$-\nabla^2\chi + \beta L^+\phi = \epsilon\chi, \qquad (3)$$

where the operator $L = -\partial/\partial x + i(\partial/\partial y)$. Problem (3) was studied in great detail for the systems without SOI (see, e.g., Stöckmann's monograph [10] or review [2]). Historically, McDonnel and Kaufmann [11] were the first to discover numerically that the complex spatial structure of real Bunimovich billiard eigenfunctions is described by the Gaussian distribution. The density probability (square of eigenfunction) statistics obeys the Porter–Thomas distribution [12]. These statistics were repeatedly observed in microwave [10, 13] and acoustic resonant [14] cavities.

In this work, we examine what happens to the statistics of two-component eigenfunctions in the presence of SOI. The energy-level statistics of a rectangular billiard, which becomes nonintegrable in the presence of SOI, was considered by Berggren and Ouchterlony in [15]. In that work, the eigenfunction node statistics were also considered and it was shown that they coincide with the statistics of nodal points of open chaotic billiards. For the numerical solution, we will use the boundary integral method [16]. A chaotic billiard was modeled by a cardioid with the boundary determined by the following equation in the Cartesian coordinate system [17]:

$$(x^2 + y^2 - \lambda^2)^2 = x^2 + y^2 + 2\lambda x + \lambda^2. \qquad (4)$$

The Bunimovich stadium was also considered. Since all results obtained for the latter do not differ from the cardioid, we present here only the cardioid results. The
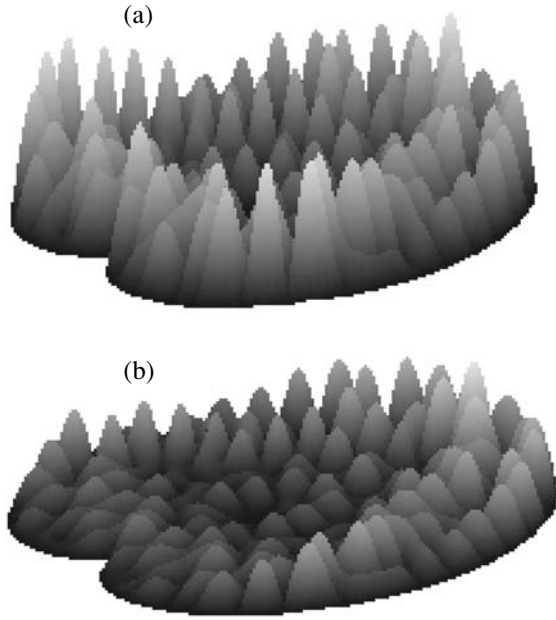
Fig. 1. Spatial structures of (a) the first $|\phi|$ and (b) the second $|\chi|$ components of the spinor eigenfunction of a cardioid with parameter $\lambda = 0.45$ for $\epsilon = 522.251$ and $\beta = 0.25$. The smallness parameter $\alpha = 0.005$.
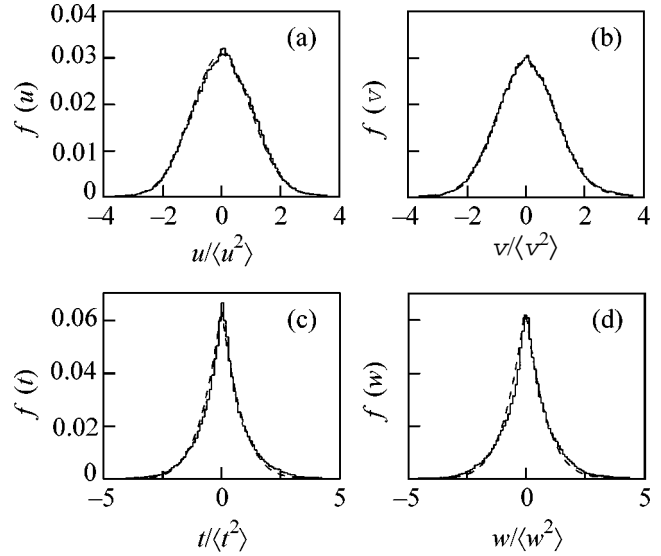

Fig. 2. Distributions of the real and imaginary parts of spinor components (7) for $\epsilon = 2509.7$ and $\beta = 0.25$. The smallness parameter $\alpha = 0.005$. The dashed curves in (a) and (b) correspond to Gaussian distribution (9). In panels (c) and (d), the dashed curves correspond to distribution (10) for $x_0 = -0.3$ and $y_0 = 0.4$.

spinor components $|\phi|$ and $|\chi|$ for the energy eigenvalue $\epsilon = 522.251$ and $\beta = 0.25$ are shown in Fig. 1. Hereafter, the cardioid parameter λ is taken to be 0.45. The number of boundary elements was chosen to be 1000. Note that, due to the Kramers theorem, all states of closed billiards with SOI are doubly degenerate. For this reason, the second degenerate state behaves exactly as shown in Fig. 1, although $|\phi|$ and $|\chi|$ should be reversed.

Although both components show chaotic behavior, there is a fundamental difference in their spatial behavior. Namely, one can see from Fig. 1 that the $|\chi|$ component is spatially nonuniform. This fact can be understood if one considers the perturbative solutions to the Schrödinger equation (3). For a free two-dimensional electron gas, the smallness parameter for SOI is given by [8]

$$\alpha = \beta k/\epsilon = \beta/\sqrt{\epsilon}, \qquad (5)$$

where k is the wave number. We will use the same parameter for a billiard. For small α, the solution to Eqs. (3) can be approximated by

$$\phi = \psi_b + O(\alpha^2),$$

$$\chi = \beta\left[\frac{1}{2}(x + iy)\psi_b + C\psi_b\right] \qquad (6)$$

$$= \frac{\beta}{2}[(x - x_0) + i(y - y_0)]\psi_b,$$

where ψ_b is the billiard eigenfunction in the absence of SOI: $-\nabla^2\psi_b = \epsilon_b\psi_b$. At first glance, the constant C can be found from the normalization condition $\int d^2\mathbf{x}(|\phi|^2 + |\chi|^2) = 1$. However, since the accuracy of the components is proportional to the SOI constant, the normalization condition includes only ψ_b that is already normalized. Because of this, the constant C (more precisely, the constants x_0 and y_0) was determined by fitting the statistics together (see below).

Solution (6) demonstrates that the second component $\chi(x, y)$ linearly increases in the billiard region, as it is clearly seen from the numerical solution shown in Fig. 1. It also follows from Eq. (6) that, if ψ_b is a random Gaussian field (RGF), the first component ϕ is also an RGF, whereas the second component χ is not. Since, in the presence of SOI, each component of the spinor eigenfunction is a complex quantity, we can represent the solution in the form

$$\begin{pmatrix} \phi(\mathbf{r}) \\ \chi(\mathbf{r}) \end{pmatrix} = \begin{pmatrix} u(\mathbf{r}) + iv(\mathbf{r}) \\ t(\mathbf{r}) + iw(\mathbf{r}) \end{pmatrix}. \qquad (7)$$

The distributions shown in Fig. 2 for all four functions demonstrate that u and v are actually the RGF, whereas the t and w statistics differ appreciably from the Gaussian distributions.

To analytically derive the distributions for the second component χ, we write, according to Eq. (6), its real part as $t(x, y) = (\beta/2)(x - x_0)\psi_b$ and the imaginary

part as $w(x, y) = (\beta/2)(y - y_0)\psi_b$. The distribution function for t is written as

$$f(t) = \langle \delta(t - t(x, y)) \rangle = \frac{1}{2\pi} \int_{-\infty}^{\infty} d\mu \langle e^{i\mu(t - t(x, y))} \rangle$$

$$= \frac{1}{2\pi} \int_{-\infty}^{\infty} d\mu \frac{1}{A} \int dx dy e^{i\mu(t - t(x, y))}, \tag{8}$$

where A is the billiard area. Assume that the eigenfunction ψ_b of a chaotic billiard is a real RGF $u(x)$. Then, by integrating Eq. (8) with the Gaussian distribution

$$f(u) = \sqrt{\frac{2\pi}{\langle u^2 \rangle}} \exp\left(-\frac{u^2}{2\langle u^2 \rangle}\right), \tag{9}$$

one obtains from Eq. (6)

$$f(t) = \frac{1}{A} \int dx dy \exp\left\{-\frac{2t^2}{\beta^2 (x - x_0)^2 \langle u^2 \rangle}\right\}. \tag{10}$$

A similar expression can be obtained for the distribution $f(w)$ of the imaginary part. Hence, the distributions for the second component χ are not universal if the Rashba SOI constant β is small, because they depend on the particular shape of a chaotic billiard. In Fig. 2, distribution (10) obtained by the numerical integration with $\beta = 0.25$ is shown by the dashed line. The constants x_0 and y_0 were found by fitting analytic distributions (10) to their numerical values. The results presented in the caption to Fig. 2 coincide with the results obtained for the constant C through the direct numerical solution of Eq. (2).

The numerically calculated matrix

$$K = \begin{pmatrix} \langle u^2 \rangle & \langle uv \rangle & \langle ut \rangle & \langle uw \rangle \\ \langle vu \rangle & \langle v^2 \rangle & \langle vt \rangle & \langle vw \rangle \\ \langle tu \rangle & \langle tv \rangle & \langle t^2 \rangle & \langle tw \rangle \\ \langle wu \rangle & \langle wv \rangle & \langle wt \rangle & \langle w^2 \rangle \end{pmatrix} \tag{11}$$

$$= \begin{pmatrix} 0.292 & 0.038 & -0.024 & -0.015 \\ 0.038 & 0.198 & -0.015 & 0.011 \\ -0.024 & -0.015 & 0.005 & 0 \\ -0.015 & 0.011 & 0 & 0.004 \end{pmatrix},$$

where $\langle F \rangle = \frac{1}{N} \sum_j F(j)$ and N is the number of points inside the billiard (200 000 in these computations) indicates that the second component is strongly correlated with the first one. In the numerical computations, we assumed that the eigenstate is normalized; i.e.,
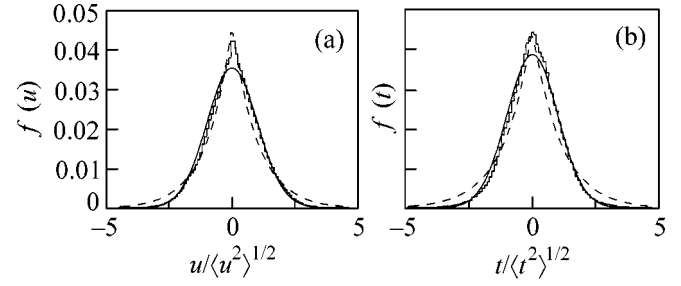
$$\sum_j (|\phi(j)|^2 + |\chi(j)|^2) = 1.$$

Fig. 3. Distributions of the real parts of the cardioid eigenstates for $\epsilon = 2501.6$ and $\beta = 2$. The SOI smallness parameter is $\alpha = 0.04$. The solid curves correspond to Gaussian distribution (9). The dashed curves correspond to distribution (10) for $x_0 = -0.050$.
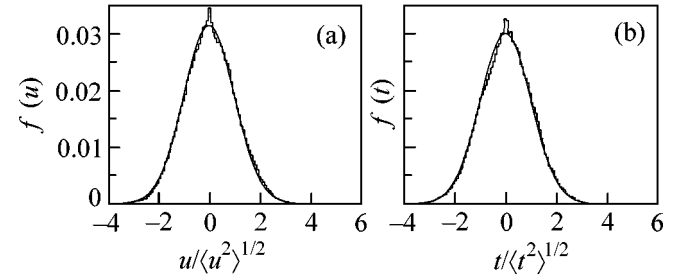

Fig. 4. Distributions of the real part of the cardioid eigenstates for $\epsilon = 2497.4$, $\beta = 10$, and $\alpha = 0.2$. The solid curves correspond to Gaussian distribution (9).

The distributions of real components u and t of spinor eigenstate (7) are shown in Fig. 3 for a moderate value $\beta = 2$ of the SOI constant. These distributions indicate that, with an increase in small parameter α, the statistics remains Gaussian for large wave-function amplitudes and is added by nonuniversal statistics (10) at small amplitudes. The statistics of the imaginary parts v and w are exactly the same as for the real eigenstate parts. For this reason, they are not shown in Fig. 3 (or Fig. 4).

In the opposite case $\alpha \gg 1$, one can ignore the kinetic energy operators in Eq. (3). Then, surprising as it may seem, Schrödiner equation (3) again reduces to the Laplace equation for both components ϕ and χ

$$L^+ L \begin{pmatrix} \phi \\ \chi \end{pmatrix} = -\nabla^2 \begin{pmatrix} \phi \\ \chi \end{pmatrix} = \beta^2 |\epsilon|^2 \begin{pmatrix} \phi \\ \chi \end{pmatrix} \tag{12}$$

with the sole difference that the eigenvalues are now equal to $\beta^2 \epsilon^2$. Hence, both components are equivalent in that they are RGFs with identical variances. The numerical solutions for $\beta = 100$ fully confirm this conclusion. However, at $\beta \geq 10$, all four functions in eigenspinor (7) are, practically, RGFs, as it is seen from Fig. 4.

Correlation matrix (11) was calculated for $\epsilon = 2499.2$, $\beta = 10$, and $\alpha = 0.2$ to give

$$K = \begin{pmatrix} 0.248 & -0.042 & 0.047 & 0 \\ -0.042 & 0.243 & 0 & 0.047 \\ 0.047 & 0 & 0.253 & 0.021 \\ 0 & 0.047 & 0.021 & 0.255 \end{pmatrix}. \qquad (13)$$

This matrix shows that, at $\beta \geq 10$, all amplitudes become almost mutually independent RGFs with the same distributions.

We now estimate the small parameter α for the quantum dots based on the semiconductor GaSb/InAs/GaSb heterostructure, for which the SOI constant is the greatest among the known systems: $\hbar^2 K = 9 \times 10^{-7}$ meV cm and $m^* = 0.055m$ [5]. Substituting these data into the SOI constant $\beta = 2m^*KR = \hbar^2 K/E_0 R$ and $E_0 = \hbar^2/2m^*R^2$, one finds that only the quantum dots with sizes $R \sim 10$ μm have $\beta \sim 10$, for which, as shown in Fig. 4, all eigenspinor components are described by the RGF. The electron Fermi energy in the dot should not exceed 1 meV. Note that $R \sim 10$ μm is the limiting attainable size for which the electron motion can be assumed to be ballistic. For the quantum dots of micron size or smaller, the eigenfunction statistics in spin–orbit problem (1) are described by nonuniversal distribution (10).

REFERENCES

1. J. H. Davies, *The Physics of Low-Dimensional Semiconductors* (Cambridge Univ. Press, Cambridge, 1998).
2. Y. Alhassid, Rev. Mod. Phys. **72**, 895 (2000).
3. E. I. Rashba, Fiz. Tverd. Tela (Leningrad) **2**, 1224 (1960) [Sov. Phys. Solid State **2**, 1109 (1960)].
4. E. A. de Andrada e Silva, G. C. La Rocca, and F. Bassani, Phys. Rev. B **55**, 16293 (1997).
5. J. Luo, H. Munekata, F. F. Fang, and P. J. Stiles, Phys. Rev. B **41**, 7685 (1990).
6. J. Nitta, T. Akasaki, H. Takaynagi, and T. Enoki, Phys. Rev. Lett. **78**, 1335 (1997).
7. J. P. Heida, B. J. van Wees, J. J. Kuipers, *et al.*, Phys. Rev. B **57**, 11911 (1988).
8. A. V. Moroz and C. H. W. Barnes, Phys. Rev. B **60**, 14272 (1999).
9. E. N. Bulgakov and A. F. Sadreev, Phys. Rev. B **66**, 075331 (2002).
10. H.-J. Stöckmann, *Quantum Chaos: An Introduction* (Cambridge Univ. Press, Cambridge, 1999).
11. S. W. McDonald and A. N. Kaufmann, Phys. Rev. Lett. **42**, 1189 (1979); Phys. Rev. A **37**, 3067 (1988).
12. N. Rosenzweig and R. Thomas, Phys. Rev. **120**, 1698 (1960).
13. A. Kudrolli, V. Kidambi, and S. Sridhar, Phys. Rev. Lett. **75**, 822 (1995).
14. K. Schaadt, MS Thesis (The Niels Bohr Inst., Univ. of Copenhagen, 1997).
15. K.-F. Berggren and T. Ouchterlony, Found. Phys. **31**, 233 (2001).
16. R. J. Riddel, Jr., J. Comput. Phys. **31**, 21 (1979); J. Comput. Phys. **31**, 42 (1979).
17. M. Robnik, J. Phys. A: Math. Gen. **16**, 3971 (1983).

Translated by V. Sakun

Quantum Zeno Effect in Cooper-Pair Transport through a Double-Island Josephson System[¶]

A. Shnirman[1] and Yu. Makhlin[1, 2]

[1] *Institut für Theoretische Festkörperphysik, Universität Karlsruhe, D-76128 Karlsruhe, Germany*
[2] *Landau Institute for Theoretical Physics, Russian Academy of Sciences, Moscow, 117940 Russia*
e-mail: shnirman@tfp.uni-karlsruhe.de
Received September 1, 2003

Motivated by recent experiments, we analyze transport of Cooper pairs through a double-island Josephson qubit. At low bias in a certain range of gate voltages, coherent superpositions of charge states play a crucial role. Analysis of the evolution of the density matrix allows us to cover a wide range of parameters, including situations with degenerate levels, when dissipation strongly affects the coherent eigenstates. At high noise levels, the so-called Zeno effect can be observed, which slows down the transport. Our analysis explains certain features of the I–V curves, in particular, the visibility and shape of resonant peaks and lines. © *2003 MAIK "Nauka/Interperiodica".*

PACS numbers: 74.50.+r; 03.65.Xp; 85.25.Cp

Among various proposals for the realization of qubits, solid-state devices appear particularly promising, since they can be easily scaled up to large qubit registers and integrated in electronic circuits [1]. Recent experiments have demonstrated quantum coherent oscillations in Josephson-junction devices. However, in such devices, due to the host of microscopic modes, decoherence processes are more difficult to control, and understanding of the decoherence mechanisms requires further analysis. Further, improvements of the quantum measurement procedure are needed to allow monitoring of the qubit's state with little influence on the qubit's dynamics before the readout. Here, we analyze recent experiments [2, 3], in which the dissipative dynamics of a Josephson charge qubit was probed by Cooper-pair transport. This experiment provides data for understanding of the dissipation in typical superconducting charge devices, and its analysis is similar to that for quantum charge detectors.

We focus on the analysis of Josephson circuits in the charge limit, in which the typical electrostatic energy needed to charge a superconducting island ($\sim (2e)^2/2C_\Sigma$, where C_Σ is the total capacitance) is higher than the Josephson energy, which controls the charge tunneling. If the system is biased close to a point where two charge states with lowest energies are degenerate, at low temperatures and operation frequencies one can neglect the higher charge states, and the system reduces to two levels (qubit). The matrix element between these levels is controlled by Josephson tunneling. In the simplest design, a Cooper-pair box [4], the quantum state of this qubit can be manipulated by voltage and current pulses

[5]. The measurement of the quantum state can be performed, for example, by coupling the qubit to a single-electron transistor (SET) and monitoring its current [1]. Here, we study a circuit, which can be described as a charge qubit inside a SET. Transport in this device probes typical time scales of the qubit dynamics, and its analysis may show new possibilities to perform the readout. Our results explain experimentally observed features of transport (the visibility and shape of resonant lines and peaks) and predict new specific behavior in a low-bias regime, in which coherent properties of the double-island qubit are probed.

The circuit and its description. Following the experimental work [2, 3], we study the system shown in Fig. 1. It consists of a Josephson junction, with a relatively strong coupling E_J, connected to further superconducting leads via weaker junctions, with $\tilde{E}_J \ll E_J$. The transport is controlled by a bias V between the external leads and gate voltages V_{g1}, V_{g2}, with gate
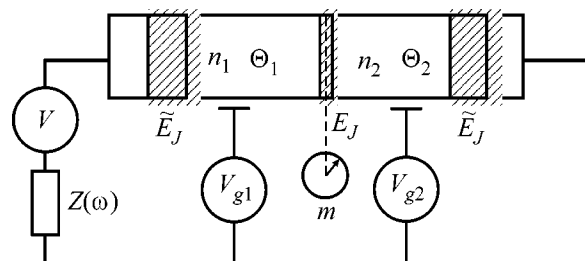

Fig. 1. The double-island system.

[¶] This article was submitted by the authors in English.

capacitances much lower than those of the junctions, $C_g \ll C_J$. The transport of Cooper pairs through a similar system with a single island between the leads (a superconducting SET) was studied, for instance, in [6–9]. Transport at a finite bias implies dissipation, which can be provided by various mechanisms. Here, we focus on low voltages and temperatures, at which the contribution of quasiparticles is negligible [3]. We study the influence of the electromagnetic environment, i.e., effective impedances in the circuit. Since $C_g \ll C_J$, the impedance of the transport voltage circuit is expected to dominate dissipation (see Fig. 1).

In [7–9], the analysis was limited to the evolution of occupations of the eigenstates (the diagonal entries of the density matrix in the eigenbasis of the nondissipative Hamiltonian). The dynamics were described in terms of incoherent transitions between these states. This approach is sufficient as long as fluctuations provide only a weak perturbation (the incoherent rates are lower than the coherent level splittings). However, in a system with almost degenerate eigenstates, this approach may fail, since the system crosses over to the so-called Zeno regime [10]. To illustrate this concept, we consider a situation relevant for the analysis below: often the charge transport may be described as a chain of transitions between various charge configurations. Under certain conditions, one link in this chain is a pair of degenerate charge states, with the coupling δ between them, coupled by incoherent transitions, with rate ~Γ, to further states. As long as δ ≫ Γ transport within the pair is fast, and the current magnitude is set by Γ. However, if the coupling δ becomes weaker than Γ, the dynamics change dramatically: frequent "observation" (fast dephasing) by the transitions destroys the coherence and slows down the evolution. The system is blocked for a long time in one of the charge states in the pair, with the typical transition rate ~δ^2/Γ, which now sets the current magnitude. The density matrix of the two-state system quickly becomes diagonal in the charge basis, while in the eigenbasis diagonal and off-diagonal entries of the density matrix are strongly coupled (cf. [1]). In order to describe the behavior of the system in both limits, we analyze the system using the master equation for the evolution of all entries of the density matrix.

We describe the state of the system by the charges en_1, en_2 of the central islands and introduce the charge em transferred across the system of three junctions (see below for a precise definition). In the Hamiltonian,

$$H = H_C + H_J + H_{\text{diss}},　　　　　(1)$$

the charging part is given by

$$H_C = \frac{(en_- + C_g V_{g-})^2}{4(3C_J + C_g)} + \frac{(en_+ + C_g V_{g+})^2}{4(C_J + C_g)} - Q_{\text{int}} V, \quad (2)$$

where

$$n_\pm \equiv n_1 \pm n_2, \quad V_{g\pm} \equiv V_{g1} + V_{g2},$$

and

$$Q_{\text{int}} \equiv \frac{en_-(2C_J + C_g)}{2(3C_J + C_g)} + \frac{en_+ C_g}{2(C_J + C_g)} + em \quad (3)$$

is the charge operator that couples to the voltage source. The Josephson part of the Hamiltonian is

$$H_J = -\tilde{E}_J(\cos\theta_1 + \cos\theta_2) - E_J \cos(\theta_2 - \theta_1 + \Psi_m), (4)$$

where θ_1, θ_2 are the phase drops across the left and the right junctions, respectively, and $\exp(i\Psi_m)$: $|m\rangle \mapsto |m + 2\rangle$ is the counting ladder operator. One can see from Eq. (4) that tunneling of a Cooper pair across the central junction changes m by 2.

Finally, the dissipative part of the Hamiltonian reads (cf. [11, 12])

$$H_{\text{diss}} = \frac{(Q_{\text{int}} - q)^2}{2C_{\text{int}}} + \sum_\alpha \left[\frac{q_\alpha^2}{2C_\alpha} + \frac{\hbar^2(\phi_\alpha - \phi)^2}{e^2 \, 2L_\alpha} \right]. \quad (5)$$

Here, ϕ is the phase drop across the impedance $Z(\omega)$ and C_{int} is the capacitance between its leads. The linear environment is presented here as a parallel connection of LC-oscillators, with the constraint

$$Z^{-1}(\omega) = \sum_{\alpha, \pm} [iL_\alpha(\omega \pm \omega_\alpha + i0)]^{-1},$$

where $\omega_\alpha = 1/\sqrt{L_\alpha C_\alpha}$.

We obtained a Hamiltonian description in terms of the phases θ_1, θ_2, ϕ and the conjugate charges en_1, $-en_2$, and q, the latter being the total charge passed through the voltage source relative to the equilibrium charge $C_{\text{int}}V$ on the plates of the capacitor C_{int}. At the relevant low frequencies, the interaction with the bath reduces to $H_{\text{int}} = -Q_{\text{int}}\delta V$, where $\delta V \equiv (q - m)/C_{\text{int}}$ is the fluctuating part of the transport voltage. A dissipative Hamiltonian of the form (5) provides for the proper high-frequency regularization of the effective bosonic bath, with cutoff frequency $\omega_c = (RC_{\text{int}})^{-1}$, where R is the real part of $Z(\omega)$.

Qualitative analysis of the low-voltage resonances. In this section, we provide qualitative analysis of the transport properties and illustrate the discussion by the results of a numerical simulation described below. We study resonances at transport voltages below the superconducting gap, $eV < \Delta$, but assume that the voltage is high enough so that the features related to the supercurrent through the system are not relevant. The discussion and figures correspond to a positive bias $V > 0$. To understand the origin of possible resonances, let us first discuss the stability diagram for the charge states (see Fig. 2), neglecting the Josephson couplings.

In the unbiased case, the stability conditions define a honeycomb pattern in the gate–voltage plane. Inside each hexagon, a certain charge state has the minimal energy. At the vertices, three charge states are degenerate. When a transport voltage V is applied, these points grow into triangles, within which the system is unstable with respect to sequential tunneling of Cooper pairs: $|0, 2, m\rangle \longrightarrow |0, 0, m\rangle \longrightarrow |2, 0, m\rangle \longrightarrow |0, 2, m + 2\rangle$ .... (In the experimentally relevant limit of Josephson couplings and temperatures below the charging energy, in the vicinity of one vertex, only three charge states $|n_1, n_2\rangle$ are relevant: $|2, 0\rangle$, $|0, 2\rangle$, and $|0, 0\rangle$.) However, this gives a low current since the incoherent tunneling through the left and right junctions $\tilde{E}_J$ is slow.

A much higher current can be achieved in resonant situations. One can expect resonant points (peaks) and lines in the $V_{g\pm}$-plane. At the peaks, defined by two constraints on $V_{g\pm}$, three charge states are in resonance. On the lines, only two charge states are degenerate. The resonant conditions determine the positions of possible peaks and lines. To evaluate the current at the resonant peaks, we note that, for typical parameters, the bottleneck of transport is associated with the incoherent transitions between triples of resonant states; the rate of these transitions is given by the golden rule and defines the current. However, the analysis of the shape of the peaks/lines (the decay of current away from resonances) is more subtle. It may require the analysis of the Zeno regime and of the crossover to this regime. Below, we develop a suitable master-equation approach. We begin with a qualitative discussion of the results.

Consider, for instance, the three-state resonance shown in Fig. 3, which corresponds to the upper vertex of the triangle in Fig. 2. In this case, the Cooper pairs tunnel incoherently in the central junction only, and coherently through two other junctions. The coherent couplings $\tilde{E}_J$ exceed the rate of incoherent transitions, which can be evaluated using the golden rule:

$$\Gamma_r \approx \frac{4\pi}{9} \frac{R}{R_Q} \frac{E_J^2}{2eV},$$ (6)

where $R_Q \equiv h/(2e)^2$, and we assumed $T \ll 2eV$. This rate defines the current magnitude at resonance, $2e\Gamma_r$.

Tuning the gates away from this resonance peak, one may still keep two levels degenerate along a resonant line. For instance, one may lift the state $|0, 0, m\rangle$ with respect to the degenerate $|0, 2, m\rangle$ and $|2, 0, m\rangle$ (see Fig. 3; if $|0, 0\rangle$ descends, the system may get Coulomb-blocked in this state). In this configuration, the transport involves a second-order coherent tunneling (cotunneling) $|0, 2, m\rangle \longrightarrow |2, 0, m\rangle$ and incoherent relaxation $|2, 0, m\rangle \longrightarrow |0, 2, m + 2\rangle$. To estimate the current, we evaluate the second-order coherent coupling between $|0, 2, m\rangle$ and $|2, 0, m\rangle$ and find $\delta \sim \tilde{E}_J^2/\Delta E$, where ΔE denotes the distance to the $|0, 0\rangle$-state (see Fig. 3). As
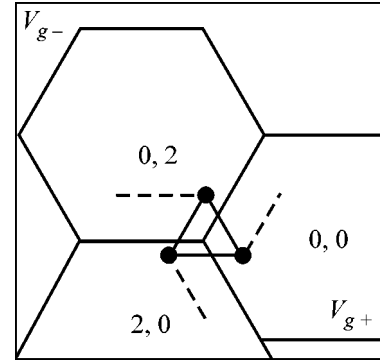

Fig. 2. The honeycomb stability diagram of charge states. The solid dots and dashed lines denote the resonance peaks and lines, respectively.
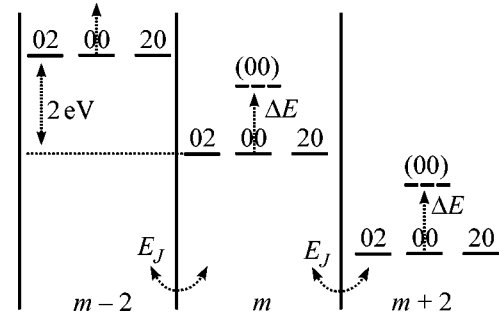

Fig. 3. Three charge levels at resonance. The (00) and dotted arrows denote a passage along a resonant line.

discussed above, the current remains to be $2e\Gamma_r$ as long as $\delta > \Gamma_r$. However, for $\delta < \Gamma_r$, the system is in the Zeno regime, and the relaxation rate $|2, 0\rangle \longrightarrow |0, 2\rangle$ defines the current $\sim 2e\delta^2/\Gamma_r$. Thus, along the resonant line, the current stays at the peak level and then drops fast. The deviation from the peak at which the current drops can be estimated from the condition $\delta \sim \Gamma_r$; further behavior is governed by the Zeno physics. For the typical parameters [2] (see below), this gives a very short line (it is also very narrow, cf. below). This may explain why this resonant line was not detected.

If the threefold degeneracy in Fig. 3 is lifted in other ways (with two states still in resonance), the transport involves higher-order incoherent processes and the current is much weaker [3]. However, there exist other resonant peaks, which are located at two lower vertices of the triangle: one can say that in Fig. 3 the voltage drops at the central junction, but it can also drop at the left/right junction. The respective rate of incoherent Cooper-pair tunneling can be evaluated using Eq. (6) with the substitution $E_J \longrightarrow \tilde{E}_J$, i.e., the current at these peaks is much lower. However, our analysis shows that the resonance lines originating from these peaks are
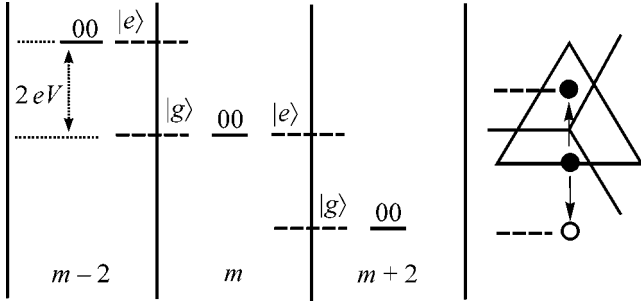
Fig. 4. Resonances with the double-island's eigenstates. The right panel shows the peaks' positions in the $V_{g\pm}$-plane. A peak emerges at $V = E_J/2e$ (the solid dot in the middle) and splits as the bias V increases. The dashed lines show the cotunneling resonances.

much longer (and wider, cf. below) and may reach the neighboring hexagons' vertices, as was indeed found experimentally. The reason is that at these peaks the incoherent rate is much lower, the coherent coupling stronger, and only at a greater distance away from the peak does the coherent coupling fall below the incoherent rate (crossover to the Zeno regime). Thus, we find, in agreement with the experimental data, that only oblique (but not horizontal) resonant lines should be visible and allow us to evaluate the shape of the resonances.

The widths of the resonant lines were evaluated in a similar way, with results in at least semi-quantitative agreement with the experimental data. We remark that the width is not set by the condition of resonance as such (which requires a charge-level splitting lower than the coupling and would define very narrow lines [3]). In fact, during the separation of two resonant states, the transport changes from coherent to incoherent. At this crossover point, the incoherent rate is higher than the respective Γ_r. Only at a greater distance from the line does it drop below Γ_r and slow the transport. The respective width scales linearly with V, similar to the experiment [2].

So far, we analyzed transport at voltages V much higher than the Josephson couplings and used the charge basis. Now, we focus on transport at lower voltages and find that, due to the coherent Josephson coupling of the charge states, the triple resonance of Fig. 3 appears only at voltages above a certain threshold.

At lower $2eV \sim E_J$, it is convenient to work in the eigenbasis of the double island. Near the triangle in Fig. 2, the difference U in charging energies of the states $|2, 0, m\rangle$ and $|0, 2, m + 2\rangle$ is small, and one finds the ground and excited eigenstates of the double island,

$$|g, m + 2\rangle = \cos\gamma|2, 0, m\rangle + \sin\gamma|0, 2, m + 2\rangle,$$

$$|e, m\rangle = -\sin\gamma|2, 0, m\rangle + \cos\gamma|0, 2, m + 2\rangle,$$

where $\tan 2\gamma = E_J/U$.

The respective resonance configuration is shown in Fig. 4. Since the minimal energy splitting between the ground and excited states is E_J, the resonant conditions of Fig. 4 require $2eV \geq E_J$. At $V = E_J/2e$, the peak is located at the lower side of the triangle (see Fig. 4). Above this threshold, the equation $E_e - E_g = E_J/\sin 2\gamma = 2eV$ ($0 < \gamma < \pi/2$) has two solutions, and the peak splits: the main peak with $\gamma > \pi/4$ enters the triangle, and the other, secondary peak ($\gamma < \pi/4$) leaves it. At strong bias $2eV \gg E_J$, the main peak reaches the upper vertex of the triangle, while the secondary becomes very narrow and joins one of the oblique resonant lines. (Note that the triangle itself slides and grows with the increase of V.)

Let us estimate the current magnitude at these resonances. The relaxation rate $|e, m\rangle \longrightarrow |g, m + 2\rangle$ is given by Eq. (6), and the matrix element between the states $|e, m\rangle$ and $|g, m\rangle$ to $|0, 0, m\rangle$ due to H_J is $E_{coupl} = (\tilde{E}_J/2)\sin\gamma$, of order $\tilde{E}_J$ for the main resonance • and weaker, $\sim \tilde{E}_J E_J/(2eV)$, for the other one.

If $\tilde{E}_J \gg (R/R_Q)E_J$, the incoherent relaxation inside the double-island is the bottleneck (the slowest stage) of the transport for both peaks, $\Gamma_r \ll E_{coupl}$, i.e., the peak height is $I_{max} \approx 2e\Gamma_r$. However, the peaks' sizes are different due to different E_{coupl} and can be found from an analysis similar to that shown above. The external peak ○ is much narrower at $2eV \gg E_J$.

For $\tilde{E}_J \ll (R/R_Q)E_J$, one finds that $\Gamma_r \gg E_{coupl}$ for the secondary peak, and also for the main resonance at voltages V close to $E_J/2e$. The Zeno effect is expected under these circumstances [10], the transport is slowed down, and transitions in the outer junctions define the current $I_{max} \sim 2e E_{coupl}^2/\Gamma_r$.

Master equation and numerics. The dynamics reduce to propagation along the chain of eigenstates with decreasing energy and growing m. To evaluate the current, we analyze the dynamics of the reduced density matrix $\hat{\sigma}$, retaining the indices n_1, n_2, m and tracing over the environment's degrees of freedom. Using the real-time Keldysh diagrammatic technique (cf. [13, 14]), we find the master equation

$$\frac{d}{dt}\hat{\sigma}(t) - L_0\hat{\sigma}(t) = \int_{-\infty}^{t} dt' \Sigma(t - t')\hat{\sigma}(t'), \qquad (7)$$

with the bare Liouville operator $L_0 \equiv i[\cdot, H_0]$, $H_0 \equiv H_C + H_J$. In the first (Born) approximation, we obtain

$$\Sigma(t) = \alpha'(t)L_{int}e^{L_0 t}L_{int} - i\alpha''(t)L_{int}e^{L_0 t}M_{int}, \qquad (8)$$

where $\alpha(t) = \alpha'(t) + i\alpha''(t)$ is given by

$$\alpha(t) \equiv (2e)^2\langle\delta V(t)\delta V(0)\rangle = \int\frac{d\omega}{\pi}\frac{J(\omega)e^{-i\omega t}}{1 - e^{-\hbar\omega/k_B T}}, \qquad (9)$$

the low-frequency spectral density $J(\omega) = 2\pi\omega R/R_Q$, and $L_{int} \equiv i[\cdot, Q_{int}/2e]$, $M_{int} \equiv i[\cdot, Q_{int}/2e]_+$. The last term in Eq. (8) violates the translational symmetry $m \longrightarrow m + 2$. The invariance is restored after a regularization, due to the counterterm $Q_{int}^2/2C_{int}$ in Eq. (5) (cf. [15]).

We label the entries of the self-energy matrix Σ by four triples $\nu^{\mp}$ and $\nu'^{\mp}$, where, e.g., $\nu^- = (n_1^-, n_2^-, m^-)$. Here, the sign $\mp$ refers to a Keldysh branch; the (un)primed indices refer to the time t' (t). Most of these indices vary over finite ranges. Indeed, only the lowest charge states n_1, n_2 participate in the low-frequency dynamics, and strongly off-diagonal entries, with large $m^- - m^+$ and $m'^- - m'^+$, are suppressed. The regularized self-energy is translationally invariant and does not depend on the sum $m^- + m^+ + m'^- + m'^+$. The Fourier transform with respect to $(m^- + m^+ - m'^- - m'^+)/2$ gives a finite matrix for each value of k.

We use the Laplace-transformed master equation: $s\hat{\sigma}(k, s) - \hat{\sigma}_0(k) = \Pi(s, k)\hat{\sigma}(k, s)$ to find the current $I = s^2 \langle m(s)\rangle|_{s\to 0}$, where $\langle m(s)\rangle = i\partial_k \mathrm{Tr}\,\hat{\sigma}(k = 0, s) = i\mathrm{Tr}(s - \Pi)^{-1}\partial_k\Pi(s - \Pi)^{-1}\hat{\sigma}_0|_{k\to 0}$. Here, $\Pi(k, s) \equiv L_0(k) + \Sigma(k, s)$, and $\hat{\sigma}_0$ is the initial condition. The numerical analysis can be simplified by taking the needed derivatives analytically and working in the eigenbasis of H_0. We ascribe a counting index $\tilde{m}$ to *eigenstates* (rather than charge states) and organize them into zones with fixed values of $\tilde{m}$ [7, 8]. The eigenstates of the total Hamiltonian (1) have only a finite m-spread, and one can use $\tilde{m}$ to evaluate the dc current.

In our analysis, we used the following parameters: $C_J = 0.8$ fF, $C_g = 8$ aF, $\tilde{E}_J = 25$ mK, $E_J = 0.5$ K, $R = 50\ \Omega$ [3]. Figure 5 shows the shape of two peaks and resonance lines for the bias V just above the threshold $E_J/2e \approx 21.5\ \mu$V, in agreement with the estimates above.

Discussion. In our calculation, we neglected the influence of the $1/f$ noise due to background-charge fluctuations. This very low frequency noise dominates the pure dephasing (that leads to energy fluctuations without transitions; its ohmic part is included in our numerical analysis). Our estimates show that these effects should not change the results substantially.

In conclusion, using the methods that allow one to cover the (Zeno) dynamics of coherent systems under strong dissipation, we analyzed the Cooper-pair transport through a double-island structure. We found separate peaks and resonant lines, whose visibility and shapes match the experimental observations. We further predict a double-peak structure near a threshold transport voltage, observation of which would be a probe of coherent properties of the double-island qubit.

We are grateful to E. Bibow, P. Lafarge, and L. Lévy for providing their results and for numerous discus-
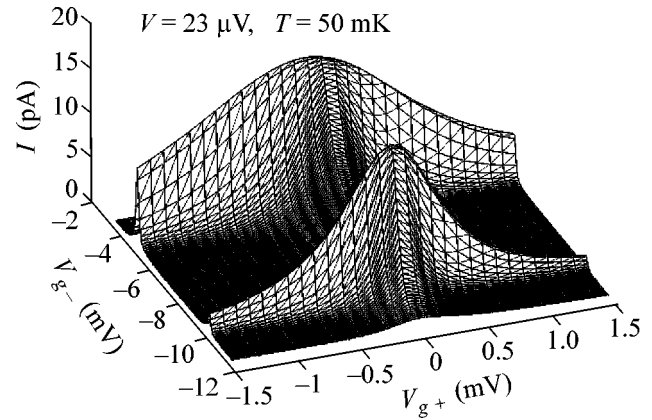

Fig. 5. $I(V_{g+}, V_{g-})$ for $V = 23\ \mu$V and $T = 50$ mK.

REFERENCES

1. Yu. Makhlin, G. Schön, and A. Shnirman, Rev. Mod. Phys. **73**, 357 (2001).

2. E. Bibow, P. Lafarge, and L. Lévy, Phys. Rev. Lett. **88**, 017003 (2002).

3. E. Bibow, PhD Thesis (Univ. Joseph Fourier, Grenoble I, 2001).

4. V. Bouchiat, D. Vion, P. Joyez, *et al.*, Phys. Scr. T **76**, 165 (1998).

5. A. Shnirman, G. Schön, and Z. Hermon, Phys. Rev. Lett. **79**, 2371 (1997); Yu. Makhlin, G. Schön, and A. Shnirman, Nature **386**, 305 (1999).

6. D. V. Averin and V. Y. Aleshkin, Pis'ma Zh. Éksp. Teor. Fiz. **50**, 331 (1989) [JETP Lett. **50**, 367 (1989)].

7. A. Maassen, J. van den Brink, G. Schön, and L. J. Geerligs, Phys. Rev. Lett. **67**, 3030 (1991).

8. A. Maassen, J. van den Brink, A. A. Odintsov, *et al.*, Z. Phys. B **85**, 459 (1991).

9. J. Siewert and G. Schön, Phys. Rev. B **54**, 7421 (1996).

10. R. Harris and L. Stodolsky, Phys. Lett. B **116**, 464 (1982).

11. G.-L. Ingold and Yu. V. Nazarov, in *Single Charge Tunneling: Coulomb Blockade Phenomena in Nanostructures*, Ed. by H. Grabert and M. H. Devoret (Plenum, New York, 1992), p. 21.

12. U. Weiss, *Quantum Dissipative Systems*, 2nd ed. (World Sci., Singapore, 1999).

13. H. Schoeller and G. Schön, Phys. Rev. B **50**, 18436 (1994).

14. Yu. Makhlin, G. Schön, and A. Shnirman, in *Exploring the Quantum-Classical Frontier*, Ed. by J. R. Friedman and S. Han (Nova Sci., Commack, N.Y., 2002), p. 405.

15. A. O. Caldeira and A. J. Leggett, Ann. Phys. (N.Y.) **149**, 374 (1983).

Spin Relaxation in the Quantized Hall Regime in the Presence of Disorder¶

S. Dickmann

Institute for Solid-State Physics, Russian Academy of Sciences, Chernogolovka, Moscow region, 142432 Russia
Weizmann Institute of Science, 76100 Rehovot, Israel
Received August 5, 2003; in final form, September 4, 2003

We study the spin relaxation (SR) of a two-dimensional electron gas in the quantized Hall regime and discuss the role of spatial inhomogeneity effects on the relaxation. The results are obtained for small filling factors ($\nu \ll 1$) or when the filling factor is close to an integer. In either case, SR times are essentially determined by a smooth random potential. For small ν, we predict a "magneto-confinement" resonance manifested in the enhancement of the SR rate when the Zeeman energy is close to the spacing of confinement sublevels in the low-energy wing of the disorder-broadened Landau level. In the resonant region, the *B*-dependence of the SR time has a peculiar nonmonotonic shape. If $\nu \simeq 2n + 1$, the SR is going nonexponentially. Under typical conditions, the calculated SR times range from 10^{-8} to 10^{-6} s. © *2003 MAIK "Nauka/Interperiodica"*.

PACS numbers: 72.25.Rb; 73.43.Cd

1. In order for the relaxation of electron spins to occur, two conditions have to be met: the first one is the presence of an interaction mixing different spin states in the system studied; the second is the availability of a mechanism which makes the relaxation process irreversible. Both conditions can be realized in a rich variety of ways, and even in the case of two-dimensional (2D) electrons, one finds a wide scatter of experimental data [1] and theoretical results [2–10] devoted to spin relaxation (SR) problems. Besides, in the magnetic field, the SR process is actually the relaxation of the Zeeman energy $|g\mu_B B \Delta S_z|$ (**B** $\parallel \hat{z}$, $\Delta S_z = S_z - S_0$ is the spin deviation of the S_z component from the equilibrium value S_0).

Theoretically, the relaxation problem of a flipped spin in a semiconductor heterostructure in a high perpendicular magnetic field seems to have been first formulated by Frenkel [4], who considered the relativistic part of the phonon field acting directly on electron spin as the interaction mixing the electron spin states. One could estimate that, in the case of another mechanism due precisely to the spin–orbit (SO) coupling reformulated for the 2D case [2, 3], the relevant spin-flip transition matrix element is greater by at least one order of magnitude. However, the work [4] caused some misunderstandings even almost a decade after its publication (see [9] and references therein).

Any properties of a 2D electron gas (2DEG) in the quantum Hall regime crucially depend on the filling factor $\nu = N/N_\phi$, where N and $N_\phi = L^2/2\pi l_B^2$ are the numbers of electrons and magnetic flux quanta, respectively

($L \times L$ is the 2DEG area, l_B is the magnetic length). In this article, we consider the SR problem in two formulations.

First, we solve the problem of one-electron spin flip in the presence of a random potential, and in so doing we study the SR in a lateral quantum dot in a high magnetic field, where the effects of interplay between the localization and the Zeeman coupling are essential. We emphasize that we deal with a weak confinement in the presence of strong *B*. Therefore, much smaller energies are relevant (~1 K) than, e.g., in the case of the usual interplay of Fock–Darwin states [11]. (The latter is based on competition of confinement and cyclotron energies which are $\gtrsim 10$ K.) The most striking manifestation of the "magneto-confinement" effect occurs when the single-electron Zeeman energy is close to the spacing of lowest-energy levels in a quantum dot or in a potential minimum. This results in strong enhancement of the SR rate. The studied one-electron problem is actual for small filling factors, $\nu \ll 1$, but, in strong magnetic fields, it may also be extended in terms of the Hartree–Fock approach to a vicinity of an even filling factor, when $\nu \simeq 2n$.

Second, we report on the results for the SR in a strongly correlated 2DEG when it presents a quantum Hall ferromagnet (QHF), i.e., when the filling factor ν is close to an odd integer ($\nu \simeq 2n + 1$). In this case, we study a new mechanism of relaxation of the total 2DEG spin, where the cause of irreversibility is neither electron–phonon interaction [6] nor inter-spin-wave scattering [7] but a disorder. We will see that, in real experimental regimes, this disorder relaxation channel must significantly prevail over the phonon one.

¶ This article was submitted by the author in English.

In both SR problems, the temperature is assumed to be equal to zero which actually means that it is lower than the single-electron Zeeman energy $\epsilon_Z = |g|\mu_B B$.

2. We consider a smooth random potential (SRP) as the disorder. The total single-electron Hamiltonian is thereby as follows: $\mathcal{H} = \hbar^2 \hat{\mathbf{q}}^2 / 2m_e^* - \epsilon_Z \hat{\sigma}_z / 2 + u(\mathbf{r}) + H_{SO} + U_{e-ph}$, where $\hat{\mathbf{q}} = -i\nabla + e\mathbf{A}/c$ and $\mathbf{r} = (x, y)$ are 2D vectors, $u(\mathbf{r})$ is the SRP field, the H_{SO} and U_{e-ph} terms respond to the SO and electron–phonon interactions (see below). If the SRP is assumed to be Gaussian, then it is defined by the correlator $K(\mathbf{r}) = \langle u(\mathbf{r})u(0) \rangle$. We choose also $\langle u(\mathbf{r}) \rangle = 0$ which means that the SRP energy is measured from the center of the Landau level. In terms of the correlation length Λ and Landau level width Δ, the correlator is

$$K(\mathbf{r}) = \Delta^2 \exp(-r^2/\Lambda^2). \qquad (1)$$

In the realistic case, $\Delta \sim 10$ K, $\Lambda \sim 30$–50 nm; therefore, $\Delta \gtrsim \hbar^2/m_e^* \Lambda^2$. We study the case $\Delta \ll \hbar\omega_c$ (ω_c is the cyclotron frequency) and $\Lambda \gg l_B$. In the SRP field, the electron drifts quasi-classically along an equipotential line. However, before the spin flip, it relaxes to an SRP minimum. Estimates for this relaxation time (due to phonon emission without any spin flip) yield values not exceeding 1 ns.

For simplicity, we model the SRP in the vicinity of a minimum by a parabolic confinement potential $u = m_e^* \omega^2 r^2/2$, and to describe the electron states, we use the symmetric gauge basis ($\mathbf{A} = \mathbf{r} \times \mathbf{B}/2$):

$$|n, m, \sigma\rangle = \sqrt{\frac{n!}{(n+m)!}} \frac{e^{-im\varphi - r^2/4a^2}}{a\sqrt{2\pi}}$$
$$\times \left(\frac{ir}{\sqrt{2}a} \right)^m L_n^m(r^2/2a^2)|\sigma\rangle, \qquad (2)$$

where L_n^m is a Laguerre polynomial; note also that only the states with $n + m \geq 0$ are considered in the following. Regarding the length a, $a = (\hbar/2m_e^* \Omega)^{1/2}$ should be substituted, where $\Omega = \sqrt{\omega^2 + \omega_c^2/4}$. The system thus becomes equivalent to a lateral quantum dot [8, 10], and we deal with the Fock–Darwin states [11] with energies $E_{n,m} = \hbar(2n + m + 1)\Omega - \hbar\omega_c m/2$. The appropriate quantity is also the level spacing $\delta = \hbar(\Omega - \omega_c/2) \approx \hbar\omega^2/\omega_c$, concerning the $m \geq 0$ states which belong to the same number n. We calculate the total rate of the transition of an electron initially occupying the upper spin sublevel to any final state of the lower spin sublevel. At first sight, we should consider the spin-flipped state $|0, 0, \downarrow\rangle$ as the initial one. However, a correction of the states due to the SO coupling has to be taken into account. We use the SO Hamiltonian specified for the (001) GaAs plane: $H_{SO} = \alpha(\hat{\mathbf{q}} \times \hat{\boldsymbol{\sigma}})_z + \beta(\hat{q}_y \hat{\sigma}_y - \hat{q}_x \hat{\sigma}_x)$.

This expression is a combination of the Rashba term [2] (with the coefficient α) and the crystalline anisotropy term [3, 5–10] ($\hat{\sigma}_{x,y,z}$ are the Pauli matrices). Assuming that α and β are small ($\alpha, \beta \ll \hbar\omega_c l_B$), we find, after perturbative treatment, the spin-orbitally corrected states before and after the spin flip:

$$|i\rangle = C_{1,1}|0, 0, \downarrow\rangle + C_{2,1}|0, 1, \uparrow\rangle$$
$$+ \frac{\beta}{\hbar\Omega\sqrt{2}a}|1, -1, \uparrow\rangle, \qquad (3)$$

$$|f_m\rangle = C_{1,m}|0, m, \uparrow\rangle + C_{2,m}|0, m-1, \downarrow\rangle$$
$$- \frac{i\alpha}{\hbar\Omega\sqrt{2}a}|1, m-1, \downarrow\rangle$$
$$+ \frac{\beta\delta\sqrt{m+1}}{\hbar\Omega\sqrt{2}a(\delta + \epsilon_Z)}|1, m+1, \downarrow\rangle, \qquad (4)$$

where $0 \leq m < \epsilon_Z/\delta$ (the Zeeman energy ϵ_Z has been neglected as compared to $\hbar\omega_c$). The coefficients $C_{i,m}$ are defined as follows: let $T = \alpha\delta\sqrt{2}/a\hbar\Omega(\epsilon_Z - \delta)$ and $P_m = 2\sqrt{1 + T^2 m}$, then $C_{1,m} = \sqrt{1/2 + 1/P_m}$ and $C_{2,m} = i \, \mathrm{sgn}(\delta - \epsilon_Z)\sqrt{1/2 - 1/P_m}$. Here, the resonance mixing of the "spin-up" and "spin-down" states (if $\epsilon_Z \simeq \delta$) has been properly taken into account. Note that the behavior of the states (3), (4) in the vicinity of the resonance (namely, in the interval $\Delta B/B \lesssim \alpha\sqrt{m_e^*/\hbar^3\omega_c} \lesssim 0.1$) is governed only by the Rashba SO mechanism.

In the resonance region, $C_{1,1} \sim |C_{2,1}|$, and $|i\rangle$ is thereby a well-hybridized spin state. The $|i\rangle \longrightarrow |f_0\rangle$ transition then is not due to the SO coupling, and this should lead to the SR enhancement. The final state $|f_0\rangle$ is the almost "pure" spin-state. In fact, we may always set $C_{1,m} = 1$ and $C_{2,m} = 0$ in the expression for $|f_m\rangle$. Indeed, though the spin hybridization of the $|f_1\rangle$ state is significant, it plays a negligible role in the SR process because of vanishing of the relevant phonon momentum $(\epsilon_Z - \delta)/c_s$. Then, we find the matrix element $\langle f_m|U_{e-ph}|i\rangle$ and, using the Fermi golden rule, obtain the SR rate within a certain SRP minimum,

$$1/\tau_\omega = \frac{2\pi}{\hbar} \sum_{m, \mathbf{k}} |\langle f_m|U_{e-ph}|i\rangle|^2 \delta(\hbar c_s k - \epsilon_Z).$$

Here,

$$U_{e-ph}(\mathbf{r}) = (\hbar/V)^{1/2} \sum_s \tilde{U}_s(\mathbf{q}, k_z)e^{i\mathbf{q}\mathbf{r}},$$

where the index s labels phonon polarization, V is the sample volume, and $\tilde{U}_s$ is the renormalized (in the 2D layer) vertex, which includes the deformation and piezoelectric fields created by the phonon [6, 12]. The
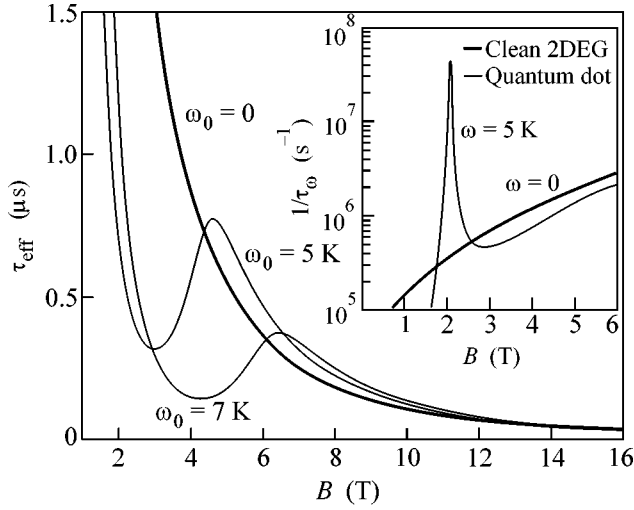
Calculations of SR time τ_{eff} in a 2DEG are carried out for $\alpha = \beta/3 = 10^{-6}$ K cm and $c_s = 3.37 \times 10^5$ cm/s (other material parameters are given in the text). In the inset, the position of the SR peak corresponds to the condition $\epsilon_Z = \delta$. The evolution of B-dependences of the spin relaxation time τ_{eff} with the parameter ω_0 is shown in the main picture.

summation over s involves averaging over directions of the polarization unit vector for both components of the electron–phonon interaction, and this may be reduced to $\left|\sum_s U_s\right|^2 = \pi\hbar c_s k/p_0^3 \tau_A(\mathbf{k})$, where $\tau_A^{-1} = \tau_D^{-1} + 5\tau_p^{-1} p_0^2 (q^2 k_z^2 + q_x^2 q_y^2)/k^6$ (see [6]). The nominal times for the deformation and piezoelectric interactions in GaAs are $\tau_D \approx 0.8$ ps and $\tau_P \approx 35$ ps [6, 12]. The nominal momentum is $p_0 = 2.52 \times 10^6$ cm^{-1} [12]. (We also refer to [6, 12] for details concerning the meaning of these quantities and their expressions in terms of the GaAs material parameters.) Finally, in the general expression for $1/\tau_\omega$, we perform the summation and, after a routine treatment, arrive at the result

$$\frac{1}{\tau_\omega} = \frac{1}{8ap_0\tau_p}\int_0^1 \frac{d\xi}{\sqrt{1-\xi}} \sum_{0 \le m < \epsilon_Z/\delta} \frac{b_m}{m!}[\mathscr{A}_m^2(\xi) + \mathscr{B}_m^2(\xi)]$$

$$\times (S_m + 5\xi - 35\xi^2/8)e^{-\xi b_m^2}\left(\frac{\xi b_m^2}{2}\right)^m, \tag{5}$$

where

$$b_m = a\frac{\epsilon_Z - m\delta}{\hbar c_s}, \quad S_m = \frac{b_m^2 \tau_p}{(ap_0)^2 \tau_d},$$

$$\mathscr{A}_m = \left(\frac{2m}{b_m\sqrt{\xi}} - \sqrt{\xi}b_m\right)|C_{2,1}| + \frac{\alpha b_m}{\hbar\Omega a}\sqrt{\frac{\xi}{2}}\,\text{sgn}(\delta - \epsilon_Z),$$

$$\mathscr{B}_m = \frac{\beta b_m}{\hbar\Omega a}\sqrt{\frac{\xi}{2}}\left(1 - C_{1,1}\frac{\delta}{\delta + \epsilon_Z}\right).$$

The estimate for α and β depends on the effective layer width [2, 3]. The rate $1/\tau_\omega$ as a function of B at $\omega = 5$ K is shown in the inset of the figure for realistic parameters indicated in the caption.

At $\omega = 0$ (i.e., in the "clean" limit), the summation in formula (5) is carried out over all numbers $m = 0, 1, \ldots, \infty$, and expression (5) is reduced to

$$\frac{1}{\tau_0} = \mathscr{V}\int_0^1 \frac{\xi d\xi}{\sqrt{1-\xi}}e^{-b^2\xi/2}(S + 5\xi - 35\xi^2/8), \tag{6}$$

where

$$\mathscr{V} = \frac{\epsilon_Z^3(\alpha^2 + \beta^2)}{4p_0\hbar^5\omega_c^2 c_s^3 \tau_p} \propto B, \quad b = \frac{\epsilon_Z l_B}{\hbar c_s} \propto \sqrt{B},$$

$$S = \frac{\tau_p \epsilon_Z^2}{\tau_D(\hbar c_s p_0)^2} \propto B^2.$$

The bold curves in the inset and in the main picture of the figure show the corresponding B-dependences.

Note that, if $\epsilon_Z = 0$, then, at any $\mathbf{r}_0$, the projection $\mathscr{P}(\mathbf{r}_0) = \langle f_m|\delta(\mathbf{r} - \mathbf{r}_0)|i\rangle$ vanishes when calculated at a finite ω in the leading order in the SO constants. (It does not occur for the "clean" states, i.e., if in Eqs. (3) and (4) we pass to the $\omega \longrightarrow 0$ limit before equating ϵ_Z to zero.) Such a vanishing is a manifestation of the general feature [8, 10]: at zero Zeeman energy, the effects of the SO coupling in the leading order and of the orbital magnetic field are similar. In particular, in a quantum dot (where $\delta > \epsilon_Z$!), the first-order SO approximation in the $\epsilon_Z \longrightarrow 0$ limit results only in a small rotation of eigenstates in the spin space. With decreasing B, we get $\mathscr{P} \propto B^{3/2}$ (if $\epsilon_Z \ll \delta \ll \omega_c$) and obtain a sharper fall of the relaxation rate as compared to the "clean" case (6).

In the presence of the SRP, we have to carry out averaging $1/\tau_{eff} = \int_0^\infty d\omega F(\omega)/\tau_\omega$, where the distribution function $F(\omega)$ is the probability that the confinement frequency will take a certain value ω. One may prove that, in the case of a Gaussian potential $u(\mathbf{r})$, it should be chosen in the form

$$F(\omega) = \frac{2\omega}{\sqrt{\pi}\omega_0}\exp(-\omega^4/4\omega_0^4).$$

(The value ω^2 is proportional to the curvature $\nabla^2 u$, and a routine analysis yields $\omega_0 = 6^{1/4}(\Delta/m_e^*)^{1/2}/\Lambda$.) Calculating $1/\tau_{eff}$ with this function, we obtain the final result (see figure). As it has to be, in comparison with τ_ω, the resonant behavior of $1/\tau_{eff}$ is smoothed, but, at actual values of ω_0, it results in nonmonotonic B-dependence of τ_{eff}. Beyond the resonance region, the behavior is as follows: (i) at small magnetic fields (when $\epsilon_Z \ll \hbar\omega_0^2/\omega_c \ll \omega_c$), only one final state $|f_0\rangle$ participates in

the SR, and we find that $\tau_{\text{eff}} \propto B^{-5}$; (ii) at high fields (when $\epsilon_Z \gg \delta_0$), there is a large but finite number of possible states $|f_m\rangle$ into which the confined spin-flipped electrons could relax, and the SR time is always longer than τ_0 but approaches this with increasing magnetic field. Note that, exactly in this high-field regime, the one-electron model becomes relevant for fillings $\nu \simeq 2n$. Then, the total 2DEG spin is determined only by a small amount $|\nu - 2n|N_\phi$ of effectively "free" electrons/holes belonging to the $(n + 1)$st/nth Landau level.

3. So, the problem has been solved when the total 2DEG spin is well smaller than N_ϕ. Now, we study the opposite case: in the ground QHF state, the spin numbers attain the maximum $S = S_z = N_\phi/2$. This case is also remarkable, since, to the first order in the ratio $r_c = (e^2/\epsilon l_B)/\hbar\omega_c$, the low-lying excitation is again known exactly: these are 2D spin waves or spin excitons (SEs). The most adequate description of the SE states is realized by spin-exciton creation

$$Q_{\mathbf{q}}^\dagger = \frac{1}{\sqrt{N_\Phi}} \sum_p e^{-ipq_x l_B^2} a_{\downarrow p + \frac{q_y}{2}}^\dagger a_{\uparrow p - \frac{q_y}{2}}$$

and annihilation $Q_{\mathbf{q}} = (Q_{\mathbf{q}}^\dagger)^\dagger$ operators [13]. In this definition, $a_{\sigma p}$ stands for the Fermi annihilation operator corresponding to the $|n, p, \sigma\rangle = L^{-1/2}e^{ipy}\varphi_n(x + pl_B^2)$ state in the Landau gauge (φ_n is the nth harmonic oscillatory function). So, the one-exciton state is $Q_{\mathbf{q}}^\dagger|0\rangle$, where $|0\rangle$ stands for the ground state. At small 2D momentum ($ql_B \ll 1$), the one-exciton state has the energy $\mathscr{E}_q = \epsilon_Z + (ql_B)^2/2M_n$ (now, we need only this small momenta approximation; see also general expressions for the 2D magneto-excitons at integer filling factors in [14]). M_n is the SE mass at $\nu = 2n + 1$, namely in the $r_c \longrightarrow \infty$ limit: $1/M_0 = (e^2/\epsilon l_B)\sqrt{\pi/8}$, $1/M_1 = 7/4M_0$, …. Note that the sum $S_- = \sum_i \sigma_-^{(i)}$ lowering the spin number S_z by 1 (i labels the electrons), when considered to be projected onto the nth Landau level, is simply proportional to the "zero" exciton creation operator $Q_0^\dagger$. When the SO coupling is ignored, any state $(S_-)^N|0\rangle$ is the eigenstate independently of the r_c magnitude and of the presence of a disorder.

The SO interaction H_{SO} and the SRP field $u(\mathbf{r})$ may be accounted perturbatively as usual. Meanwhile, now the unperturbed part of the Hamiltonian involves the Coulomb interaction. For present purposes, the approximation in the context of the projection onto a single Landau level is quite sufficient (cf. [6]). We note also that the QHF state $|0\rangle$ is resistant to the SRP disorder. Such a stability is determined by the exchange energy ($\sim e^2/\kappa l_B$), which is much larger than the amplitude Δ.

There are two fundamentally different alternatives that provide the initial perturbation of spins. The first one is the perturbation of the spin system as a whole when the S number is not changed: $\Delta S = 0$, but $\Delta S_z \neq 0$. This is a Goldstone mode, which presents a quantum precession of the vector $\mathbf{S}$ around the $\mathbf{B}$ direction. In terms of the SE representation, $|\Delta S_z| = N_\phi/2 - S_z$ is the number of "zero" SEs excited in a 2DEG. Let $|\Delta S_z| = N$; the corresponding state is $(S_-)^N|0\rangle \propto (Q_0^\dagger)^N|0\rangle$, and it has the energy $N\epsilon_Z$. (Note that "zero" SEs do not interact among themselves; besides, the stability of the $(S_-)^N|0\rangle$ state with respect to the disorder is identical to that for the $|0\rangle$ state because of $u(\mathbf{r})$ and S_- commuting.) The second case of the perturbation is the $\Delta S = \Delta S_z$ type of the deviation. This does not change the symmetry and involves the excitation of "nonzero" SEs, where each SE changes the spin numbers by 1: $S \longrightarrow S - 1$, $S_z \longrightarrow S_z - 1$. In contrast to zero SEs, the nonzero ones interact. This interaction [7] and/or the direct exciton–phonon coupling [6] governs the nonzero SE annihilation which should go faster than the nonzero SE annihilation process.

The SRP inhomogeneity does not essentially affect the SE energy and the nonzero annihilation. Indeed, the exciton is neutral, and the interaction with the SRP incorporates the energy $U_{\text{x–SRP}} \sim ql_B^2\Delta/\Lambda$ (the nonzero SE possesses the dipole momentum $el_B^2[\mathbf{q} \times \hat{z}]$; see [14]). The latter may be negative but is always smaller than the nonzero SE energy $\mathscr{E}_q$. If the SE were to annihilate, the energy conservation condition $\mathscr{E}_q + U_{\text{x–SRP}} = 0$ would not be satisfied except for at negligible rare points, where the gradient ∇u is accidentally large. Therefore, the SRP leads to only small corrections (on the order of $U_{\text{x–SRP}}/\mathscr{E}_q$) to the other mechanisms of the nonzero SE relaxation [6, 7].

A distinctly different process contributes to the SR in the case of the first type of the spin perturbation. This is an effective interaction of zero SEs among themselves arising due to the SO coupling [6]. Such an interaction does not preserve the total number of excitons N: at an elementary event, two zero excitons merge into one nonzero (the spin momenta change following the rule $S_z \longrightarrow S_z + 1$, $S \longrightarrow S - 1$). In other words, the SO coupling and the SRP field mix the initial $|i\rangle = (Q_0^\dagger)^N|0\rangle$ and the final $|f_q\rangle = Q_{\mathbf{q}}^\dagger (Q_0^\dagger)^{N-2}|0\rangle$ states. These "many-exciton" states have to be normalized (see the normalization factors in [6, 13]). So, the SRP plays the same role as the phonon field studied previously [6]. Now, the energy conservation condition takes the form $2\epsilon_Z \approx \mathscr{E}_q$, where the interaction of nonzero SE with the SRP is ignored as compared to other members of this equation. If solving this for q, we obtain $q = q_0 \equiv \sqrt{2M_n\epsilon_Z}/l_B$.

The detailed calculation of the SR rate is truly similar to that performed in [6]. Indeed, the Fourier expansion $u(\mathbf{r}) = \sum_{\mathbf{q}} \bar{u}(q)e^{i\mathbf{q}\mathbf{r}}$ looks like the phonon field created by "frozen" (of zero frequency) phonons. Then, this SRP field and the SO Hamiltonian are treated perturbatively. In so doing, it is convenient to present them in terms of the excitonic operators. We calculate the relevant matrix element between the $|i\rangle$ and $|f_q\rangle$ normalized states and obtain $\left|\mathcal{M}_{i \to f_q}\right|^2 = N^2(\alpha^2 + \beta^2)|q\bar{u}(q)|^2/(\hbar\omega_c)^2 N_\phi$. Finally, again with the use of the Fermi golden rule, we find after summation over all states $|f_q\rangle$ that the SR rate takes the same form as in the case of the phonon mechanism [6], $dS_z/dt = (\Delta S_z)^2/\tau_{SRP}N_\phi$, but incorporates a different time constant:

$$\tau_{SRP}^{-1} = \frac{16\pi^2(\alpha^2 + \beta^2)M_n^2\epsilon_Z\bar{K}(q_0)}{\hbar^3\omega_c^2 l_B^4}.$$

Here, $\bar{K}$ stands for the Fourier component of the correlator [the equivalence $\bar{K}(q) = L^2|\bar{u}(q)|^2/4\pi^2$ has been employed]. The SR follows the law

$$\Delta S_z(t) = \frac{\Delta S_z(0)}{1 + t|\Delta S_z(0)|/\tau_{sr}N_\phi},$$

where $\tau_{sr}^{-1} = \tau_{ph}^{-1} + \tau_{SRP}^{-1}$, because the relaxations of both types proceed in parallel. A natural question is: *What is the ratio of the times τ_{ph} and τ_{SRP}?* If $T \lesssim \hbar c_s q_0$ (in fact, this means that $T \lesssim 1$ K) and $B < 15$, then the SR time τ_{ph} depends weakly on T and B. In particular, at $\nu = 1$, we find that $\tau_{ph} \simeq 10$ μs [6, 7]. The ratio of interest is determined only by the Fourier component $\bar{K}(q_0)$:

$\tau_{ph}/\tau_{SRP} = 0.24\pi\tau_p p_0 \Delta^2\Lambda^2 e^{-\Lambda^2 q_0^2/4}/\hbar^2 c_s$ (for $\bar{K}$, we have substituted the value calculated with help of Eq. (1)). So, for the actual parameters $\tau_{ph}/\tau_{SRP} \sim 100$–1000, i.e., exactly the "disorder" time ($\tau_{SRP} \sim 10^{-8}$–10^{-7} s) governs the breakdown of this Goldstone mode. In conclusion, we underline that the relaxation is going nonexponentially and the actual time is increased by a factor of $N_\phi/\Delta S_z(0)$.

REFERENCES

1. M. Dobers, K. von Klitzing, J. Sneider, *et al.*, Phys. Rev. Lett. **61**, 1650 (1988); S. Bar-Ad and I. Bar-Joseph, Phys. Rev. Lett. **68**, 349 (1992); V. Srinivas, Y. J. Chen, and C. E. C. Wood, Phys. Rev. B **47**, 10907 (1993); V. E. Zhitomirskii, V. E. Kirpichev, A. I. Filin, *et al.*, JETP Lett. **58**, 439 (1993); B. W. Alphenaar, H. O. Müller, and K. Tsukagoshi, Phys. Rev. Lett. **81**, 5628 (1998).

2. Yu. A. Bychkov and E. I. Rashba, JETP Lett. **39**, 78 (1984).

3. M. I. D'yakonov and V. Yu. Kachorovskii, Sov. Phys. Semicond. **20**, 110 (1986).

4. D. M. Frenkel, Phys. Rev. B **43**, 14228 (1991).

5. G. Bastard, Phys. Rev. B **46**, 4253 (1992).

6. S. M. Dikman and S. V. Iordanskii, JETP **83**, 128 (1996).

7. S. M. Dikman and S. V. Iordanskii, JETP Lett. **70**, 543 (1999).

8. A. V. Khaetskii and Y. V. Nazarov, Phys. Rev. B **61**, 12639 (2000).

9. A. V. Khaetskii, Phys. Rev. Lett. **87**, 049701 (2001).

10. I. L. Aleiner and V. I. Fal'ko, Phys. Rev. Lett. **87**, 256801 (2001).

11. V. Fock, Z. Phys. **47**, 446 (1928); C. G. Darwin, Proc. Cambridge Philos. Soc. **27**, 86 (1930).

12. V. F. Gantmakher and Y. B. Levinson, *Carrier Scattering in Metals and Semiconductors* (Nauka, Moscow, 1984; North-Holland, Amsterdam, 1987).

13. The excitonic operators appeared originally in publications of A. B. Dzyubenko and Yu. E. Lozovik, Sov. Phys. Solid State **25**, 874 (1983); Sov. Phys. Solid State **26**, 938 (1984); in the paper of J. Phys. A **24**, 415 (1991) these authors considered the many-exciton states and calculated the norms.

14. I. V. Lerner and Yu. E. Lozovik, Sov. Phys. JETP **53**, 763 (1981); Yu. A. Bychkov, S. V. Iordanskii, and G. M. Eliashberg, JETP Lett. **33**, 143 (1981); C. Kallin and B. I. Halperin, Phys. Rev. B **30**, 5655 (1984).

Adsorbate Vibrational Mode Enhancement of Radiative Heat Transfer¶

A. I. Volokitin[1, 2] and B. N. J. Persson[1]

[1] Institut für Festkörperforschung, Forschungszentrum, Jülich D-52425, Germany
[2] Samara State Technical University, Samara, 443100 Russia
Received June 26, 2003; in final form, September 4, 2003

We show that radiative heat transfer between two solid surfaces at short separation may increase by many orders of magnitude when the surfaces are covered by adsorbates. In this case, the heat transfer is determined by resonant photon tunneling between adsorbate vibrational modes. We propose an experiment to check the theory. © 2003 MAIK "Nauka/Interperiodica".

PACS numbers: 78.20.Ci; 78.68.+m; 44.40.+a

It is well known that for bodies separated by $d \gg d_T = c\hbar/k_B T$, the radiative heat transfer between them is described by the Stefan–Boltzmann law

$$S = \frac{\pi^2 k_B^4}{60\hbar^3 c^2}(T_1^4 - T_2^4), \qquad (1)$$

where T_1 and T_2 are the temperatures of solids **1** and **2**, respectively. In this limiting case, the heat transfer is connected with traveling electromagnetic waves radiated by the bodies and does not depend on the separation d. For $d < d_T$, the heat transfer increases by many orders of magnitude due to the evanescent electromagnetic waves that decay exponentially into the vacuum; this is often referred to as photon tunneling. At present, there is an increasing number of investigations of heat transfer due to evanescent waves in connection with scanning probe microscopy under ultrahigh vacuum conditions [1–7]. It is now possible to measure extremely small amounts of heat transfer into small volumes [8]. Scanning tunneling microscope (STM) can be used for local heating of the surface, resulting in local desorption or decomposition of molecular species, and this offers further possibilities for the STM to control local chemistry at the surface.

The efficiency of the radiative heat transfer depends strongly on the dielectric properties of the media. In [3, 5, 6], it was shown the heat flux can be greatly enhanced if conductivities of the material are chosen to maximize the heat flow due to photon tunneling. At room temperature, the heat flow is maximal at conductivities corresponding to semimetals. In fact, only a thin film (~10 Å) of a high-resistivity material is needed to maximize the heat flux [5]. Another enhancement mechanism of the radiative heat transfer can be connected with resonant photon tunneling between states localized on the different surfaces. Recently, it was discovered that resonant photon tunneling between surface plasmon modes give rise to extraordinary enhancement of the optical transmission through subwavelength hole arrays [9]. The same enhancement of surface modes can be expected for the radiative heat transfer (and the van der Waals friction [10]) if the frequency of these modes is sufficiently low to be excited by thermal radiation. At room temperature, only the modes with frequencies below ~10^{13} s^{-1} can be excited. Recently, enhancement of the heat transfer due to resonant photon tunneling between surface plasmon modes localized on the surfaces of the semiconductors was predicted [7]. Other surface modes, which can be excited by thermal radiation, are adsorbate vibrational modes.

In this paper, we study the radiative heat transfer between small particles, e.g., adsorbed molecules, or dust particles, considered as point dipoles, and situated on the surfaces of different bodies. Using an electromagnetic approach, in the dipolar approximation, we derive a general expression of the radiative heat power exchanged between the particles. We show that if the particles have resonance frequencies which are matched, the heat transfer can be enhanced by many orders of magnitude in comparison with the heat transfer between clean surfaces of good conductors.

Let us consider two particles with dipole polarizabilities $\alpha_1(\omega)$ and $\alpha_2(\omega)$ and with the fluctuating dipole moments p_1^f and p_2^f normal to the surfaces. According to fluctuation–dissipation theorem [11], the spectral density function for the fluctuating dipole moment is given by

$$\langle p_i^f p_j^f \rangle_\omega = \frac{\hbar}{\pi}\left(\frac{1}{2} + n_i(\omega)\right)\mathrm{Im}\,\alpha_i(\omega)\delta_{ij} \qquad (2)$$

where the Bose–Einstein factor

$$n_i(\omega) = \frac{1}{e^{\hbar\omega/k_B T_i} - 1} \tag{3}$$

applies. Assume that the particles are situated opposite each other on two different surfaces, at temperatures T_1 and T_2, respectively, and separated by the distance d. The fluctuating electric field of a particle **1** does work on particle **2**. The rate of work is determined by

$$P_{12} = 2\int_0^\infty d\omega\omega\mathrm{Im}\alpha_2(\omega)\langle E_{12}E_{12}\rangle_\omega \tag{4}$$

where E_{12} is the electric field created by particle **1** at the position of particle **2**:

$$E_{12} = \frac{8p_1^f/d^3}{1 - \alpha_1\alpha_2(8/d^3)^2}. \tag{5}$$

From Eqs. (2)–(4), we get P_{12}, and the rate of cooling of particle **2** can be obtained using the same formula by reciprocity. Thus, the total heat exchange power between the particles is given by

$$P = P_{12} - P_{21}$$
$$= \frac{2\hbar}{\pi}\int_0^\infty d\omega\omega\frac{\mathrm{Im}\alpha_1\mathrm{Im}\alpha_2(8/d^3)^2}{\left|1 - (8/d^3)^2\alpha_1\alpha_2\right|^2}(n_1(\omega) - n_2(\omega)). \tag{6}$$

Let us firstly consider some general consequences of Eq. (6). There are no constraints on the particle polarizability $\alpha(\omega) = \alpha' + i\alpha''$ other than that α'' is positive, and α' and α'' are connected by the Kramers–Kronig relation. Therefore, assuming identical surfaces, we are free to maximize the photon-tunneling transmission coefficient

$$t = \frac{(8\alpha''/d^3)^2}{\left|1 - (8\alpha/d^3)^2\right|^2}. \tag{7}$$

This function is a maximum when

$$\alpha'^2 + \alpha''^2 = (d^3/8)^2 \tag{8}$$

so that $t = 1/4$. Substituting this result in (6) gives the upper boundary for the heat transfer power between two particles as

$$P_{\max} = \frac{\pi k_B^2}{3\hbar}(T_1^2 - T_2^2). \tag{9}$$

This result is a particular case of the more general statement [3] which says that there is a maximum heat flow in a given channel. A simple interpretation can be given for Eq. (9). The energy transfer between the particles can be considered as a result of the collisions. The maximal rate of energy transfer is of the order of magnitude of the product of the characteristic thermal energy on the frequency of the collision, equal to the maximal frequency of the vibration which can be thermally excited, thus $P_{\max} \sim k_B T k_B T/\hbar$. For adsorbed molecules at the concentration $n_a = 10^{19}$ m^{-2}, when one surface is at the temperature of zero and the other is at room temperature, the maximal heat flux due to the adsorbates $S_{\max} = n_a P_{\max} = 10^{12}$ W/m^2, which is nearly ten orders of magnitude larger than the heat flux due to black body radiation, $S_{BB} = \sigma T = 4 \times 10^2$ W/m^2.

We rewrite the denominator of the integrand in Eq. (6) in the form

$$\left|1 - (8\alpha/d^3)^2\right|^2 = [(1 - 8\alpha'/d^3)^2 + (8\alpha''/d^3)^2]$$
$$\times [(1 + 8\alpha'/d^3)^2 + (8\alpha''/d^3)^2]. \tag{10}$$

The conditions for resonant photon tunneling are determined by equation

$$\alpha'(\omega_\pm) = \pm d^3/8. \tag{11}$$

Close to resonance, we can write

$$(1 \pm 8\alpha'/d^3)^2 + (8\alpha''/d^3)^2 \approx$$
$$(8\beta_\pm/d^3)^2[(\omega - \omega_\pm)^2 + (\alpha''/\beta_\pm)^2], \tag{12}$$

where

$$\beta_\pm = \frac{d\alpha_r'(\omega)}{d\omega}\bigg|_{\omega = \omega_\pm}.$$

Assuming $|\alpha''/\beta_\pm| \ll \omega_\pm$, we get the following contribution to the heat transfer:

$$P = \frac{\hbar}{2}[(\alpha''(\omega_+)/|\beta_+|)\omega_+(n_1(\omega_+) - n_2(\omega_+))$$
$$+ (+ \longrightarrow -)]. \tag{13}$$

Close to a pole, we can use the approximation

$$\alpha \approx \frac{a}{\omega - \omega_0 - i\eta}, \tag{14}$$

where a is a constant. Then, from the resonant condition (11), we get

$$\omega_\pm = \omega_0 \pm 8a/d^3.$$

For the two-poles approximation to be valid, the difference $\Delta\omega = |\omega_+ - \omega_-|$ must be greater than the width η of the resonance, so that $8a/d^3 > \eta$.

For $\eta \ll 8a/d^3$, from Eq. (6) we get

$$P = \frac{\hbar\eta}{2}[\omega_+(n_1(\omega_+) - n_2(\omega_+)) + (+ \longrightarrow -)]. \tag{15}$$

Using Eq. (15), we can estimate the heat flux between identical surfaces covered by adsorbates with concentration n_a: $S \approx n_a P$. Interesting, the explicit d dependence has dropped out of Eq. (15). However, P may still be d-dependent, through the d-dependence of $\omega_\pm$. For

$\hbar\omega_{\pm} \leq k_B T$, the heat transfer will only be weakly distance independent.

For $8a/d^3 < \eta$, we can neglect multiple scattering of the photons between the particles, so that the denominator in the integrand in Eq. (6) equals unity. For $d \gg l$, where l is the interparticle spacing, the heat flux between two surfaces covered by adsorbates with concentration n_{a1} and n_{a2} can be obtained after integration of the heat flux between two separated particles. We get

$$S = \frac{24\hbar n_{a1} n_{a2}}{d^4} \int_0^\infty d\omega\, \omega \,\text{Im}\alpha_1 \text{Im}\alpha_2 [n_1(\omega) - n_2(\omega)]. \quad (16)$$

Assuming that α can be approximated by Eq. (14), for $\omega_0 \ll \eta$, Eq. (16) gives the heat flux between two identical surfaces:

$$S = \frac{12\pi\hbar\omega_0 a^2 n_a^2}{d^4 \eta} [n_1(\omega_0) - n_2(\omega_0)]. \quad (17)$$

We note that Eq. (17) can be obtained directly from the heat flux between two semi-infinite solids [3, 5, 6]. In such approach, the contribution to the heat flux from adsorbates can be taken into account by appropriate modification of the Fresnel formulas for the reflection factors [12].

For $d > d_T$, the dipole field is determined by the expression in the wave zone. The simplest way to obtain contribution of adsorbates to heat flux in this case is to use a macroscopic approach. However, without calculation, it is clear that, in this region, the surface contribution to the heat transfer due to adsorbates will be negligibly small in comparison to the volume contribution, because, in the limit of the large wavelength, the reflection amplitudes of the electromagnetic waves are reduced to classical Fresnel formulas, which do not contain information about the surface region. For black bodies, this volume contribution is determined by the Stefan–Boltzmann law. The heat transfer between the clean surfaces of good conductors was investigated in detail in [13].

In the case of ionic adsorption, the dipole polarizability is given by

$$\alpha = \frac{e^{*2}/M}{\omega^2 - \omega_0^2 - 2i\omega\eta}, \quad (18)$$

where e^* is the ionic charge, M is the ionic mass, and ω_0 and η are the vibrational frequency and damping constant, respectively. For the K/Cu(001) system, $\omega_0 = 1.9 \times 10^{13}$, and at low coverage, $e^* = 0.88$ [14], which gives $a = e^{*2}/2M\omega_0 = 7 \times 10^{-17}$ m^3/s. For $\eta = 10^{12}$ s^{-1} and $d < 10$ Å, when one surface has $T = 300$ K and the other $T = 0$ K, we get distance independent $P \approx 10^{-9}$ W. In this case, for $n_a = 10^{18}$ m^{-3}, the heat flux $S \approx 10^9$ W/m^2. With the same conditions, the heat flux between two clean surfaces $S_{\text{clean}} \approx 10^6$ W/m^2. Thus, the

photon tunneling between the adsorbate vibrational states can strongly enhance the radiative heat transfer between the surfaces.

Let us describe the physical origin of the different regimes in resonant photon tunneling between adsorbate vibrational modes. At sufficiently small separation, when $8a/d^3 > \eta$, the photons go back and forth several times in the vacuum gap, building up coherent constructive interference in the forward direction much as would occur in resonant electron tunneling. In this case, the vibrational modes on the isolated surfaces combine to form collective vibrational modes (diatomic "molecules"), where the adsorbates vibrate in phase or out of phase. This will result in a very weak distance dependence of the heat flux, because the transmission probability for a photon depends very weakly on d in this case (see above). For large d, when $8a/d^3 < \eta$, sequential tunneling is more likely to occur, where the photon excited in an adsorbate vibrational mode tunnels to the adsorbate vibration at the other surface and then couples to the other excitations in the media and exits.

The above discussion is for a special case of matching adsorbate vibrational frequencies ($\omega_1 = \omega_2 = \omega_0$), but the picture still applies in the nonsymmetric case ($\omega_1 \neq \omega_2$). Here, adsorbate vibrational modes on the two surfaces have different frequencies and, instead of a vibration mode for diatomic homopolar molecules, we have a diatomic heteropolar molecule.

Finally, let us suggest an experiment to probe the photon-tunneling heat transfer theory. Consider a solid surface (substrate) at low temperature with a low concentration of weakly adsorbed atoms (e.g., noble gas atoms) or molecules. The position of the atoms can be mapped out relative to the substrate using an STM. Next, the surface of another solid at higher temperature (e.g., room temperature) is brought in the vicinity (separation d) of the substrate. The heat transfer (via photon tunneling) to the substrate will result in a temperature increase on the substrate surface. This will result in the diffusion of the weakly bound adsorbates. The (average) diffusion distance will be a function of the heat transfer. If the two bodies are separated after a given time period, and if the new position of the adsorbates is determined using the STM [15], it is possible to infer the heat transfer from the hot to the cold surface as a function of the separation d. This experiment is conveniently performed using as the second (warm) body an atomic force microscope (AFM) with a wide flat tip, such as the type recently produced and used for studies of contact mechanics [16].

In summary, we have presented a detailed theoretical study of the heat transfer between surfaces covered by adsorbates. We have shown that resonant photon tunneling between adsorbate vibration modes can give rise to extraordinary enhanced heat transfer, in comparison with the heat transfer between clean surfaces of good conductor. This result can be used in the scanning probe microscopy for local heating and modification of

the surface. Finally, we have suggested an experiment by which the radiative heat transfer due to photon tunneling can be measured.

REFERENCES

1. D. Polder and M. Van Hove, Phys. Rev. B **4**, 3303 (1971).

2. M. L. Levin, V. G. Polevoy, and S. M. Rytov, Zh. Éksp. Teor. Fiz. **79**, 2087 (1980) [Sov. Phys. JETP **52**, 1054 (1980)].

3. J. B. Pendry, J. Phys.: Condens. Matter **11**, 6621 (1999).

4. A. Majumdar, Annu. Rev. Mater. Sci. **29**, 505 (1999).

5. A. I. Volokitin and B. N. J. Persson, Phys. Rev. B **63**, 205404 (2001); Phys. Low-Dimens. Semicond. Struct. **5/6**, 151 (2001).

6. A. I. Volokitin and B. N. J. Persson, Phys. Rev. B **65**, 115419 (2002).

7. J. P. Mulet, K. Joulin, R. Carminati, and J. J. Greffet, Appl. Phys. Lett. **78**, 2931 (2001).

8. J. R. Barnes, R. J. Stephenson, M. E. Welland, *et al.*, Nature **372**, 79 (1994).

9. A. Krishnan, T. Thio, T. J. Kim, *et al.*, Opt. Commun. **200**, 1 (2001).

10. A. I. Volokitin and B. N. J. Persson, Phys. Rev. Lett. **91**, 106101 (2003).

11. L. D. Landau and E. M. Lifshitz, *Course of Theoretical Physics*, Vol. 5: *Statistical Physics,* 2nd ed. (Nauka, Moscow, 1964; Pergamon, Oxford, 1970).

12. D. C. Langreth, Phys. Rev. B **39**, 10020 (1989).

13. P. Senet, G. Witte, and J. P. Toennies, Chem. Phys. Lett. **299**, 389 (1999).

14. M. L. Levin, V. G. Polevoy, and S. M. Rytov, Zh. Éksp. Teor. Fiz. **79**, 2087 (1980) [Sov. Phys. JETP **52**, 1054 (1980)].

15. G. Briner, M. Doering, H. Rust, *et al.*, Science **278**, 257 (1997).

16. R. Buzio, C. Boragno, F. Biscarini, *et al.*, Nat. Mater. **2**, 233 (2003).

On the Stability of a Weakly Charged Surface of Liquid Helium

V. Shikin

Institute of Solid-State Physics, Russian Academy of Sciences, Chernogolovka, Moscow region, 142432 Russia
Received September 4, 2003

The traditional approach to the development of instability of a weakly charged helium surface needs correction. It is shown that the well-known electrostatically "equipotential" Frenkel–Tonks scenario should be transformed to a more general sequence of events that would remain reasonable when the 2D charge density tends to zero. Under these conditions, the priorities change and the instability development through nucleation (with the formation of separate multicharged dimples) becomes preferable. The experiment qualitatively confirms the predictions of the theory. © 2003 MAIK "Nauka/Interperiodica".

PACS numbers: 67.55.-s

To date, the problem of instability and reconstruction of a charged helium surface has been well elaborated. The original Frenkel–Tonks results [1–3] concerning the surface oscillations and stability in a charged metallic fluid were extended by Gor'kov and Chernikova to the helium surface with 2D electrons [4, 5]. More recently, the same authors have developed the theory of equipotential reconstruction of a charged fluid surface (see [6]). They found that the flat state of a charged fluid boundary transforms to the corrugated state. The theory predicted the lattice type, the lattice parameter, the corrugation amplitude as functions of the degree of supercriticality (the excess of electric field over its critical value), etc. In this case, the perturbed fluid surface remains electrically equipotential.

In the alternative reconstruction scenario, the charged helium surface is divided into a system of isolated many-electron dimples [7]. Each of them has a charged nucleus, beyond which the fluid surface is neutral. The interaction between dimples can align them in various clusters and, in particular, cause their periodic distribution along the surface.

Despite the long-standing "coexistence" of the reconstruction variants, the priority of the equipotential scenario has not been questioned so far. This was also aided by the paper of Mel'nikov and Meshkov [8], where it was shown that the equipotential reconstruction changes to dimple reconstruction as the supercriticality increases under conditions that the total number of electrons is conserved.

The experiments performed mainly with the use of charges near the helium surface show a good agreement with predictions [1–5] about the stability boundaries of a charged fluid surface (see [9]). Later on, the most interesting (most sensitive to electron density) portion of the surface oscillation dispersion curve has been measured carefully to confirm all the expected details [10]. Finally, the existence of periodic [11] and aperiodic [12] reconstruction variants was proved for a fluid conducting boundary.

Nevertheless, one cannot assert that all is right with the scenario under discussion. First, the results of perturbative calculations of the equipotential periodic reconstruction on the assumption that the surface corrugation amplitude is smaller than the capillary length are valid only for a weakly charged helium surface in the so-called soft reconstruction regime (the perturbation amplitude is much smaller than the capillary length [6]). By the charging or the surface-filling factor one implies the ratio ν of the mean 2D-electron density n_s to its critical value n_s^{max} (see Eq. (6)). At the same time, the periodic reconstruction over the entire accessible helium surface can be experimentally observed [11] only in the vicinity of maximal values $\nu \le 1$, where a hard reconstruction regime occurs (the corrugation amplitude is scaled by the capillary length). This inconsistency, of course, would not be dramatic but that there is a second fact. At small $\nu \ll 1$, the observed reconstruction is not periodic. The helium surface is not covered here with a periodic corrugation effecting the entire liquid mirror, as it would follow from the predictions made in [6, 8]. By contrast, according to the observations in [12], the charges are grouped into one or more many-electron dimples occupying only a small portion of the helium surface. Evidently, the dimplelike reconstruction is energetically more favorable in the region $\nu \ll 1$, and this fact calls for special analysis.

It is shown in this work that, for small filling factors, the reconstruction process displays the properties of first-order phase transition. For transformations of this type, the intersection of chemical potentials of the competing phases determines a binodal stability point (line), near which the major phase nucleates in a fluctu-

Metal ——————————— h

2DEG

- - - - - - - - - - - - - - d

——————————— 0
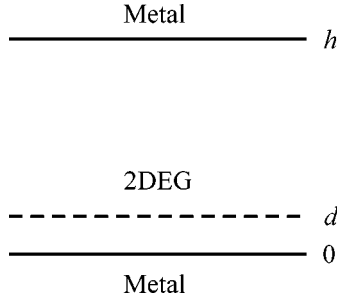
Metal

Schematic of a cell with 2D electron system and the following geometric notation: h is the separation between metallic electrodes and d is the thickness of helium film. 2D electrons are situated at the fluid surface.

ative way. With helium, this process consists in the nucleation of many-electron dimples on the background of a uniform near-critical charged surface state of a fluid. In addition, there is an absolute instability point (line) (spinodal) that appears in the dynamic equations for transition and manifests itself without any threshold expectations. For a charged liquid, spinodal coincides with the Frenkel–Tonks dynamic instability threshold. In the phase diagram, the binodal, as a rule, occupies a rather large phase volume, although the nuclei appear after a certain activation time. The spinodal transition is stimulated by an abrupt jump of any external parameter into the spinodal region in the diagram, after which the time evolution of instability should follow the characteristic exponential law. The problem of the points of coexistence of binodal and spinodal has no general solution. Sometimes they coexist and sometimes not.

If the suggested picture is true, then all the presently known experiments with the reconstruction of a weakly charged helium surface were carried out in the binodal region. In this case, only the separate dimples appear. With an increase in ν, dimples are grouped into complexes (dimple clusters) with internal periodicity. In the region $\nu \longrightarrow 1$, the cluster area tends to the total area of the liquid mirror (see figures in [12]). As to the spinodal instability mechanism, it has not yet been observed.

1. Before proceeding to the particular results, we first write the existing solution [1–5] to the problem of the electrically equipotential stability of a fluid boundary. For the system shown in the figure, electric fields E_- over and E_+ under the charged helium surface are

$$E_- = \frac{V}{h} - 4\pi\sigma\frac{d}{h}, \tag{1}$$

$$E_+ = \frac{V}{h} + 4\pi\sigma\frac{h-d}{h}, \tag{2}$$

where $\sigma = en_s$ and V is the potential difference between the cell plates (figure).

If the external field over helium is completely screened, i.e., if $E_- = 0$ and, hence,

$$4\pi\sigma = V/d, \tag{3}$$

the electric field E_+ is

$$E_+ = V/d. \tag{4}$$

Conditions (3) and (4) are fulfilled in a metallic fluid with infinite conductivity (see [1–3]). In this case, the field E_- inside the medium is zero by definition, so that the surface charge is determined by Eq. (3), as was pointed out even in the original works [4, 5] devoted to this problem. The distinguishing feature of the problems on the charged helium boundary is that the parameter n_s can be varied, starting with its infinitesimal values, independently of V. In this case, the metallic limit (3) and (4) is possible as a limiting case, although only at large ν values (for detail, see below).

In terms of E_- and E_+, the electrically equipotential stability of a charged fluid is determined by the condition

$$(4\pi en_s)^2 + (E_+ + E_-)^2 = 16\pi\kappa\alpha, \quad \kappa^2 = \rho g/\alpha, \tag{5}$$

where E_- and E_+ are given by Eqs. (1) and (2), respectively; α and ρ are, respectively, the surface tension of liquid helium and its density; g is the gravitational acceleration; and κ^{-1} is the capillary constant. In reality, the potential difference V and the electron density n_s are the independent parameters of this problem. However, since the phase diagram in the (n_s, E_-) coordinates is rather pictorial, these variables are often chosen, somewhat artificially, as independent variables.

If $E_- = 0$ (complete screening), then

$$E_+ = V/d \equiv 4\pi en_s,$$

and the maximal electron density $n_s^{\max}$ over helium is determined from Eq. (5),

$$\sigma_{\max}^2 = \kappa\alpha/2\pi, \quad (E_+^{\max})^2 = 8\pi\kappa\alpha. \tag{6}$$

By introducing the filling factor

$$\nu = \sigma/\sigma_{\max}, \tag{7}$$

one brings Eq. (5) to the form

$$\nu^2 + (\epsilon_+ + \epsilon_-)^2 = 2, \quad \epsilon_\pm = E_\pm/4\pi\sigma_{\max}. \tag{8}$$

At $\epsilon_- \longrightarrow 0$, one has

$$\nu(\epsilon_- \longrightarrow 0) \longrightarrow 1. \tag{8a}$$

In the opposite limit $\nu \longrightarrow 0$,

$$\epsilon_-(\nu \longrightarrow 0) = \epsilon_+(\nu \longrightarrow 0) \longrightarrow 1/\sqrt{2}. \tag{8b}$$

The positions of points (8a) and (8b) in the (ν, ϵ_-) plane correspond to the limiting values of the function $\nu(\epsilon_-)$.

In actuality, limit (8b) makes no real sense for function (8), because the condition for electrical equipotentiality of a distorted helium surface ceases to be fulfilled as this limit is approached. This requirement

$$\varphi = \text{const} \qquad (9)$$

should be replaced by a more general condition

$$\mu = e\varphi + \zeta = \text{const}, \qquad (10)$$

where ζ is the chemical component of the 2D charges over helium in general definition (10) of the electrochemical potential μ.

The structure of ζ in a system with finite electron density n_s is a separate problem, which now still calls for a more distinct solution. Since we present below only the qualitative conclusions and appeal only to the low electron-density limit, we use the explicit expression for ζ in the form

$$\zeta = -T\ln[n_T/n(x)], \quad n_T = mT/2\pi\hbar^2, \\ n_T/n(x) \gg 1. \qquad (11)$$

Here, T is the electron temperature coinciding with the temperature of the liquid substrate, m is the charge-carrier effective mass, and $n(x)$ is the local electron density.

In the problem on equilibrium of a charged helium surface, the dominant part (including large logarithm (11)) of condition (10) enters into the set of equations determining the spatial equilibrium of an unperturbed system "electrons + flat fluid boundary." The corresponding calculations [13, 14] provide information on the distribution of quasi-free electrons over the charged helium surface. As to the stability problem, only the perturbation $\delta\zeta(x)$ caused by the deformation of fluid boundary is significant in this case. As a result, definitions (10) and (11) for the oscillating part of the problem are simplified,

$$eE_-\xi(x) + e\varphi_-(x) - T\delta n(x)/n_s = \text{const}, \\ n(x) = n_s + \delta n(x), \\ eE_-\xi(x) + e\varphi_-(x) = eE_+\xi(x) + e\varphi_+(x), \qquad (12) \\ \int \delta n(x)dx = 0.$$

By using linearized relations (12) and the Poisson equation, one can easily determine the electric potential $\varphi_-(x)$ proportional to the small perturbation $\xi(x)$ of the fluid surface profile:

$$\varphi_-(x, z) = \varphi_-(q)e^{iqx}e^{qz}, \quad z > 0, \qquad (13)$$

$$\varphi_-(q)(1 + 2\pi e^2 n_s/qT) = 2\pi e^2 n_s(1 + eE_-/qT)\xi_q, \quad (13a)$$

where ξ_q is the Fourier component of the perturbation $\xi(x)$, with

$$\int \xi(x)dx = 0.$$

The limits of electrically equipotential approximation (9) and (8) can be estimated from Eq. (13a). This approximation is valid if

$$2\pi e^2 n_s/qT \gg 1, \qquad (14)$$

where q is the characteristic wave number of the perturbation $\xi(x)$.

In the opposite limit, the chemical part of the condition (12) for equipotentiality becomes dominant, and the dispersion law for small surface oscillations takes the form

$$\rho\omega^2/\alpha = (\kappa^2 - \eta^2)q + q^3, \quad \eta^2 = n_s E_+^2/\alpha T. \quad (15)$$

One can readily see that dispersion law (15) transforms at $\eta^2 \longrightarrow 0$ to the proper asymptotic form for $\omega(q)$ in the absence of Coulomb forces.

As in the Frenkel–Tonks problem, the oscillations with dispersion law (15) lose stability. However, this occurs in a different region, namely, at

$$\eta^2 > \kappa^2, \quad E_+ \simeq E_- \simeq V/h. \qquad (16)$$

The scale of characteristic density n_s^c separating the two limiting screening situations is given by $n_s^c \simeq 10^4$–10^5 cm^{-2} for the wave numbers on the order of capillary length and the temperature on the order of one degree.

According to Eq. (16), to make a weakly charged helium surface unstable, the field should increase as $E_\perp \propto n_s^{-1/2}$ with decreasing n_s. This statement is qualitatively different from the "equipotential" predictions (see asymptotic behavior (8b)). Consequently, the behavior of the $\epsilon_-(\nu)$ spinodal at small ν values terminates not at the point (8b) but is extended, following the root law, up to $\epsilon_- \longrightarrow \infty$.

It is worthwhile to note that instability (16) is primarily developed at small wave numbers (and not at the capillary length, as in the case of (5)).

2. In the problem of a binodal in the reconstruction process, the dimple energy competes with the electrostatic energy of a capacitor with 2D electrons filling the whole accessible fluid surface. Such a statement of this problem is ambiguous, because, in the general case, the charge of a fluctuatively appeared dimple is arbitrary. The situation is relatively simple only in the limiting case $\nu \ll 1$. The maximal energy gain corresponds to the transition of all free electrons to a single dimple. This happens in conditions where the Coulomb energy V_c of the electron subsystem occupying a circle with radius L between the capacitor plates (figure) becomes

comparable to the energy W of a many-electron dimple with the same charge Q:

$$V_c = Q^2 \frac{(h-d)d}{L^2 h}, \quad Q = \pi L^2 e n_s, \qquad (17)$$

$$W = Q^2 \kappa \left[s \exp\left(\frac{x^2}{2}\right) \text{Ei}\left(-\frac{x^2}{2}\right) - \frac{1}{x} \right], \qquad (18)$$

$$s = 1/(2\kappa R_*), \quad x = \kappa R,$$

$$R_*^2 = \sqrt{\pi}\alpha/(eE_\perp^2), \quad E_\perp \simeq V/h,$$

where $\text{Ei}(x)$ is the integral exponential function and $E_\perp$ is the electric field pressing electrons down to the surface at a finite electron density $E_\perp \simeq E_+$. The value of R in Eq. (18) is found by minimizing the energy W (18) with respect to R.

At $L \gg h$, the energy V_c (17) is rather low, so that, instead of the general (competing with V_c) expression (18) for W, one can use its expansion near the zero point

$$W(s_o, x_o) = 0, \quad s_o = 1.05, \quad x_o = 0.72,$$

$$W(s, x_o) \simeq \frac{\partial W}{\partial s_o}(s - s_o). \qquad (18a)$$

As a result, by equating the competing energies

$$Q^2 \frac{(h-d)d}{L^2 h} = \frac{\partial W}{\partial s_o}(s_{\max} - s_o), \qquad (19)$$

one determines the value of $s_{\max}$. Since the left-hand part of Eq. (19) is small, $s_{\max}$ is close to s_o.

The electric field $E_+^{\max}$, being related to $s_{\max}$ by Eqs. (18), determines the abscissa on the (ν, ϵ_-) plane (in this region, $E_\perp = E_+ \simeq E_- = V/h$) where the binodal terminates at $n_s \longrightarrow 0$. This field, of course, is independent of n_s (the quantity $n_s \propto Q$ drops out of definition (19)). Consequently, the binodal goes "under" the asymptotic curve (16) for the spinodal in the limit $n_s \longrightarrow 0$. In other words, the instability in this region should develop in a dimplelike way, which is the required result.

3. In summary, we can state that the reconstruction process at small ν values is mainly of dimple origin. In the $\nu \longrightarrow 0$ limit, the instability, being stimulated by a finite value of V/h, gives rise to an isolated dimple that accumulates all surface electrons, rather than to the periodic reconstruction. As ν increases, the number of dimples can increase to form eventually a dimple crystal, as observed experimentally in [12].

It is worth noting that the incomplete screening effect (in our case, replacement of Eq. (9) by Eq. (10)) more than once attracted the attention of researchers in the field of low-dimensional phenomena. This effect proved to be essential for the properties of quasi-one-dimensional degenerate conducting channels with a parabolic confining potential [15–18]. Simultaneous measurements of the Shubnikov–de Haas oscillations and the dipolar plasma eigenfrequency in these channels give two essentially different values for the curvatures of parabolic potentials determining the discrete electronic levels in the well and the dipolar plasma frequency ω_1 in it: k_o and $k_1 \gg k_o$. It was found that ω_1^2 is proportional to the bare curvature k_1, while the quantization of one-electron motion in the parabolic well depends on the degree of screening of the initial potential $V(x)$ forming the channel. For the quasiclassical channel width $w \gg a_b$, where a_b is the Bohr effective radius, the equilibrium electron-density profile inside the channel satisfies the requirement for electrostatic equipotentiality (requirement of the form (9)). In this case, the electron motion inside the channel is virtually nonquantized, and, hence, it has no effect on the Shubnikov–de Haas oscillations. If, however, $w \geq a_b$, the screening in the channel zone ceases to be purely coulombic, and the effective parabolic potential with curvature $k_o \leq k_1$ appears to quantize (along with a magnetic field) the electron motion and affect the Shubnikov–de Haas oscillations.

Another series of publications have been devoted to studying the screening properties of a degenerate 2D system in the vicinity of metal–insulator transition (see, e.g., [19, 20]). As expected, the requirement (9) for purely electrostatic screening of the external action changes, with a gradual decrease in electron density, to the combined requirement of form (10), with the exchange interaction playing the role of chemical addition $\zeta(n_s)$ in the degenerate systems, to give $\zeta(n_s) \propto \sqrt{n_s}$.

REFERENCES

1. Ja. Frenkel, Phys. Z. Sowjetunion **8**, 675 (1935).
2. L. Tonks, Phys. Rev. **48**, 562 (1935).
3. Ya. Frenkel', Zh. Éksp. Teor. Fiz. **6**, 347 (1936).
4. L. Gor'kov and D. Chernikova, Pis'ma Zh. Éksp. Teor. Fiz. **18**, 119 (1973) [JETP Lett. **18**, 68 (1973)].
5. D. Chernikova, Fiz. Nizk. Temp. **2**, 1374 (1976) [Low Temp. Phys. **2**, 669 (1976)].
6. L. Gor'kov and D. Chernikova, Dokl. Akad. Nauk SSSR **228**, 829 (1976) [Sov. Phys. Dokl. **21**, 328 (1976)].
7. V. Shikin and P. Leiderer, Pis'ma Zh. Éksp. Teor. Fiz. **32**, 439 (1981) [JETP Lett. **32**, 416 (1981)].
8. V. Mel'nikov and S. Meshkov, Pis'ma Zh. Éksp. Teor. Fiz. **33**, 222 (1981) [JETP Lett. **33**, 211 (1981)].
9. A. Volodin, M. Khaĭkin, and V. Édel'man, Pis'ma Zh. Éksp. Teor. Fiz. **26**, 707 (1977) [JETP Lett. **26**, 543 (1977)].
10. P. Leiderer, Phys. Rev. B **20**, 4511 (1979).

11. M. Wanner and P. Leiderer, Phys. Rev. Lett. **42**, 315 (1979).

12. P. Leiderer, W. Ebner, and V. Shikin, Surf. Sci. **113**, 405 (1982).

13. D. Chernikova, Zh. Éksp. Teor. Fiz. **68**, 249 (1975) [Sov. Phys. JETP **41**, 121 (1975)].

14. A. Dyugaev, P. Grigor'ev, and Yu. Ovchinnikov, Zh. Éksp. Teor. Fiz. **117**, 1251 (2000) [JETP **90**, 1089 (2000)].

15. K. Berggren, T. Thornton, D. Newson, and M. Pepper, Phys. Rev. Lett. **57**, 1769 (1986).

16. K. Berggren and D. Newson, Semicond. Sci. Technol. **1**, 327 (1986).

17. S. Laux, D. Frank, and F. Stern, Surf. Sci. **196**, 101 (1988).

18. V. Shikin, T. Demel, and D. Heitman, Zh. Éksp. Teor. Fiz. **96**, 1406 (1989) [Sov. Phys. JETP **69**, 797 (1989)].

19. J. Eisenstein, L. Pfeiffer, and K. West, Phys. Rev. B **50**, 1760 (1994).

20. S. Ilani, A. Yacobi, D. Mahalu, and H. Shtricman, Phys. Rev. Lett. **84**, 3133 (2000).

Translated by V. Sakun

Surface Tension of Pure Liquid Helium Isotopes

A. M. Dyugaev[1, 2] and P. D. Grigoriev[1, 3, *]

[1]*Landau Institute for Theoretical Physics, Russian Academy of Sciences, Chernogolovka, Moscow region, 142432 Russia*
e-mail: pashag@itp.ac.ru
[2]*Max-Planck-Institut for the Physics of Complex Systems, Dresden D-01187, Germany*
[3]*High Magnetic Field Laboratory, MPI-FRF and CNRS, BP166, Grenoble F-38042, France*
Received September 4, 2003

The effects caused by vapor inhomogeneity over liquid helium are considered. Both pure isotopes have surface levels, whose population increases with temperature T. We separated their contribution to the temperature dependence of surface tension $\sigma_3(T)$ and $\sigma_4(T)$ and compared our theoretical results with the results of Japanese experimental works [1–3]. For liquid He^3, one has $\sigma_3(T) = \sigma_3(0) - \alpha_3^\infty T^2$ at 0.2 K $< T < 1$ K and $\sigma_3(T) = \sigma_3(0) - \alpha_3^0 T^2 \exp(-\Delta_3/T)$ at $T < 0.2$ K, with $\Delta_3 \approx 0.25$ K. For liquid He^4, $\sigma_4(T) = \sigma_4(0) - AT^{7/3} - \alpha_4^0 T^2 \exp(-\Delta_4/T)$ at $T < 2$ K, where A is the Atkins constant and $\Delta_4 \approx 4$ K. The parameters α_3^0, α_3^∞, and α_4^0 depend on the fluid properties. © *2003 MAIK "Nauka/Interperiodica".*

PACS numbers: 67.55.Cx; 68.03.Cd

1. In works [1–4], surface tension of pure helium isotopes was studied experimentally in detail. For liquid He^4, the Atkins law [1, 5]

$$\sigma_4(T) = \sigma_4(0) - AT^{7/3} \quad (1)$$

was found to be valid at $T < 1$ K.

For liquid He^3, $\sigma_3(T)$ depends quadratically on T at 0.16 K $< T < 0.9$ K [2]:

$$\sigma_3(T) = \sigma_3(0) - \alpha_3^\infty T^2. \quad (2)$$

According to the data presented in [3], $\sigma_3(T)$ is independent of T at low temperatures $T < 0.16$ K, and the extrapolation of the law (2) for $T = 0$ has an accuracy of 3×10^{-3}. These experimental findings have been a puzzle over 15 years. As the experimental accuracy was improved, a weak maximum was revealed at $T \approx 0.1$ K in the temperature curve $\sigma_3(T)$. This nonmonotonic feature has the order of 3×10^{-4} [4].

In this work, the theory of surface tension of liquid helium is developed on the basis of a physical principle common to both isotopes over a wide temperature range. It is assumed that the localized atomic states, which will be called, by convention, the fog states, exist at the liquid–vapor interface. This term is conventional because fog can equally be related to fluid and vapor [6]. The presence of fog is evident, at least, for liquid He^4. Indeed, the nonmonotonic temperature dependence of surface tension for the solutions of helium isotopes is explained by the contribution from the bound atomic states of He^3 at the surface of liquid He^4 (Andreev impurity levels) [7]. This effect is caused by

the van der Waals attraction of He^3 atoms to the liquid He^4. Since the He^4 atom is 4/3 times heavier than the He^3 atom, He^4 should have a surface level if the latter exists for the lighter He^3 atom. In this case, the atomic statistics are immaterial, because, to a first approximation, liquid helium is a quantum nondegenerate fluid, and its surface does not distinguish between its own and foreign atoms [8, 9]. Note that, contrary to the situation considered in [7], the energy of surface levels is higher than the chemical potential. For this reason, the surface levels are not occupied at $T = 0$. The existence of surface levels is confirmed by the analysis of the experimental data on electron mobility over liquid helium. The experiment and theory are at variance in the temperature range, where, as it may seem at first glance, only the electron scattering by vapor atoms is significant [10].

2. The wave function of the expected surface state has the form

$$\psi_{\mathbf{k}}(\boldsymbol{\rho}, z) = \varphi(z)\exp(i\mathbf{k}\boldsymbol{\rho}), \quad (3)$$

where the coordinates $\boldsymbol{\rho}$ and z correspond, respectively, to the atomic movement along and transverse to the fluid surface. The boundary condition $\varphi(\infty) = \varphi(-\infty) = 0$ is the natural property of a localized surface state. Function (3) corresponds to the spectrum

$$\varepsilon(\mathbf{k}) = \varepsilon^0 + \mathbf{k}^2/2M, \quad (4)$$

where M is the effective atomic mass and ε^0 is the energy of localized level. For liquid He^3, the contribu-

tion from states (3) to the surface tension $\sigma_3(T)$ is determined by the thermodynamic potential $\Omega_3(\mu_3, T)$ [6]:

$$\sigma_3(T) = \sigma_3(0) + \Omega_3(\mu_3, T),$$

$$\Omega_3(\mu_3, T) = -2T\int \ln\left(1 + \exp\left(\frac{\mu_3 - \varepsilon_3(k)}{T}\right)\right)\frac{d^2k}{(2\pi\hbar)^2}, \quad (5)$$

where $\mu_3(T)$ is the chemical potential of liquid He³. From Eqs. (4) and (5), one obtains the following expression for Ω_3:

$$\Omega_3 = -T^2\frac{M_3}{\pi\hbar^2}\int_0^\infty \frac{x\,dx}{\exp(x + \Delta_3/T) + 1}, \quad (6)$$

where Δ_3 is the level energy measured from the chemical potential: $\Delta_3 \equiv \varepsilon_3^0 - \mu_3$. The parameter Δ_3 in Eq. (6) is to be determined by comparison between theory and experiment. To a first approximation and ignoring the temperature dependence of Δ_3, one has from Eq. (6) at $T \ll \Delta_3$

$$\sigma_3(T) = \sigma_3(0) - T^2\exp\left(-\frac{\Delta_3}{T}\right)\alpha_3^0; \quad \alpha_3^0 = \frac{M_3}{\hbar^2\pi}. \quad (7)$$

It it clear from this expression why the surface tension becomes temperature-independent at $T \ll \Delta_3 \approx 0.25$ K, as it was observed in [3]. Setting $M_3 = M_3^0$, where M_3^0 is the mass of He³ atom, one obtains numerical value $\alpha_3^0 = 27.2$ mdyne/cm².

At $T \gg \Delta_3$, one gets from Eq. (6)

$$\sigma_3(T) = \sigma_3(0) - T^2\alpha_3^\infty; \quad \alpha_3^\infty = \alpha_3^0\frac{\pi^2}{12}. \quad (8)$$

The numerical value $\alpha_3^\infty = 22.4$ is in agreement with the measured value $\alpha_3^\infty = 22.3$ [2]. The qualitative $\sigma(T)$ dependence explaining the experimental data reported in [2, 3] has the form

$$\sigma_3(T) = \sigma_3(0) - \alpha_3^\infty T^2\exp(-\Delta_3/T). \quad (9)$$

The estimate $\Delta_3^0 \approx 0.25$ K is obtained from the comparison of Eq. (7) with the experimental data [3], and the value $\mu_3(0) = -2.5$ K is the energy $\varepsilon_3^0 = \mu_3(0) + \Delta_3^0 \approx -2.25$ K of the bound surface state.

In the next approximation, one should take into account the dependence of parameter $\Delta_3^0 = \varepsilon_3^0 - \mu_3$ on T. The temperature dependence of chemical potential $\mu_3 = \mu_3(T)$ is determined using the exact equation [6]

$$\mu = \bar{F} + P/n_L, \quad (10)$$

where $\bar{F}$ is the free energy per atom, P is the pressure, and n_L is the fluid density. If the temperature is not too

high, then $P = n_v T$, where n_v is the vapor density. Since $n_v \ll n_L$, the second term in Eq. (10) is small, so that the T dependence of μ_3 can be found from the expression [6]

$$\mu_3(T) = \mu_3(0) + \int_0^T C_3(T_1)dT_1 - T\int_0^T\frac{C_3(T_1)dT_1}{T_1}, \quad (11)$$

where $C_3(T)$ is the heat capacity per one He³ atom. We first carry out the qualitative analysis of the effects responsible for the temperature dependence $\Delta_3(T)$. At low temperatures, $C_3(T) = T/T_F$, and one gets from Eq. (11)

$$\mu_3(T) = \mu_3(0) - \frac{1}{2}\frac{T^2}{T_F}, \quad (12)$$

where T_F is the He³ degeneracy temperature $T_F \cong 0.36$ K [11]. According to the theory of nondegenerate quantum liquids [8, 9], the temperature dependence of $\bar{F}$ is dominated by the spin entropy $S_\sigma = \ln 2$:

$$\mu_3(T) \approx \mu_3(0) - T\ln 2. \quad (13)$$

The temperature dependence of energy $\varepsilon_3^0(T)$ can be estimated by considering the fog nonideality in a first virial approximation:

$$\varepsilon_3^0(T) = \varepsilon_3^0(0) + V_3 n_3(T), \quad (14)$$

where V_3 is the phenomenological interaction potential between He³ atoms, and the fog density $n_3(T)$ is given by the expression

$$n_3(T) = 2\int \frac{d^2k}{(2\pi\hbar)^2}\frac{1}{\exp\left(\dfrac{\varepsilon_3(k) - \mu_3}{T}\right) + 1}. \quad (15)$$

From Eqs. (4) and (15), one obtains

$$n_3(T) = \frac{M_3 T}{\pi\hbar^2}\ln\left[1 + \exp\left(-\frac{\Delta_3}{T}\right)\right]. \quad (16)$$

The equation for the parameter $\Delta_3(T)$ follows from Eqs. (11), (14), and (16):

$$\Delta_3(T) = \Delta_3^0(T) + \lambda_3 T\ln\left[1 + \exp\left(-\frac{\Delta_3(T)}{T}\right)\right], \quad (17)$$

$$\Delta_3^0(T) = \varepsilon_3^0(0) - \mu(T), \quad \lambda_3 = V_3\frac{M_3}{\pi\hbar^2}.$$

At high temperatures $T > T_F$, one obtains from Eqs. (13) and (17)

$$\Delta_3(T) \approx \Delta_3(0) + T\ln 2$$

$$+ \lambda_3 T\ln\left[1 + \exp\left(-\frac{\Delta_3(T)}{T}\right)\right]. \quad (18)$$
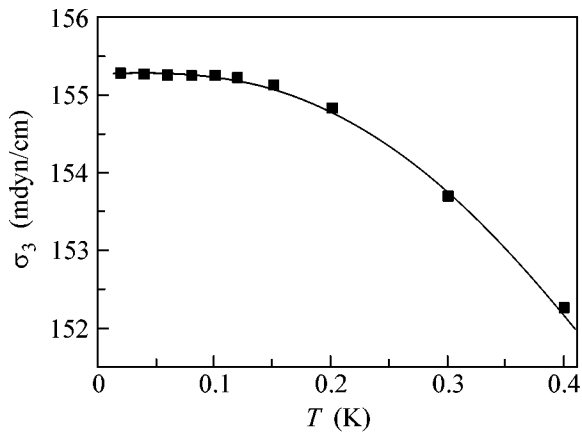
Fig. 1. Comparison of (solid line) the temperature dependence defined by Eq. (21) for the surface tension $\sigma_3(T)$ of liquid He^3 with (points) the experimental data from [2, 3] at low temperatures. The proposed theory accounts for the deviation of the $\sigma_3(T)$ dependence from the quadratic law at $T < \Delta_3^0$.
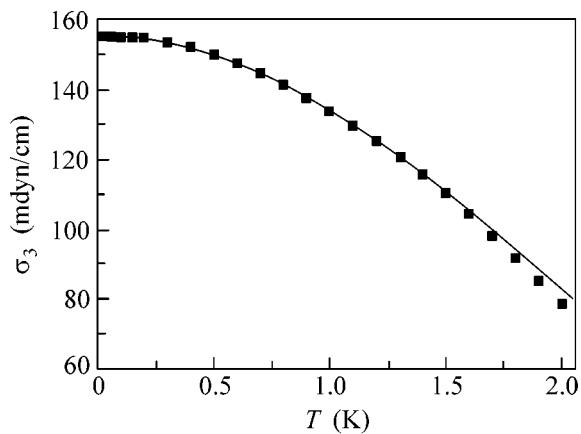

Fig. 2. Comparison of the calculated T dependence of σ_3 with the experimental data from [2, 3] over a broad temperature range.

With allowance for the smallness $\Delta_3(0) \approx 0.25$ K, it follows from Eq. (18) that $\Delta(T) \sim T$, irrespective of the sign of interaction V_3 at high $T > T_F$, and it is seen from Eqs. (5) and (6) that $\sigma_3(T) - \sigma_3(0) \sim T^2$.

Thus, allowance for the temperature dependence of the parameter Δ_3 in Eq. (6) does not contradict the experimental law (2) at high $T > T_F$. Although the parameter $\Delta_3(0)$ is found from the data [2, 3] with a very high accuracy, their is an ambiguity in the definition of λ_3 in Eq. (17) and M_3 in Eq. (6), because even the first approximation $\Delta_3 = 0$ and $M_3 = M_3^0$ is accurate to 3×10^{-3}. Next we restrict ourselves to the ideal fog model ($\lambda_3 = 0$) (17), while the temperature dependence $\mu_3(T)$

will be determined exactly using Eq. (11) and experimental data for $C_3(T)$ [11]. We present below the analytic expression for $\Delta_3(T) = \Delta_3(0) - \mu_3(T)$, because the data in [11] agree well at $T < 2$ K with the formula

$$C_3(T) = 0.2T + 0.105\frac{T}{T^2 + T_0^2}; \quad T_0 = 0.21 \text{ K} \quad (19)$$

The theoretical substantiation of Eq. (19) is given in [9]. Equations (11) and (19) are used to determine the dependence $\Delta_3 = \Delta_3(T)$:

$$\Delta_3(T) = 0.25 + 0.2T^2 + 0.5T\arctan\frac{T}{T_0}$$
$$- 0.053\ln\left(1 + \frac{T^2}{T_0^2}\right), \quad (20)$$

where temperature is in K.

Numerical integration using Eq. (11) and the data [11] for $C_3(T)$ confirms expression (20) to an accuracy of 10^{-2} at $T < 1.5$ K, and the comparison of Eqs. (5) and (6) with the experimental data for $\sigma_3(T)$ [2, 3] yields the value $M_3 = 2.25 M_3^0$ for the effective mass in the ideal fog model. With a precision of 3×10^{-4}, the dependence $\sigma_3 = \sigma_3(T)$ at $T < 0.4$ K has the form (Fig. 1)

$$\sigma_3(T) = \sigma_3(0) - \alpha_3^0 T^2 \int_0^\infty \frac{x\,dx}{\exp\left(x + \frac{\Delta_3}{T}\right) + 1}, \quad (21)$$

where $\sigma_3(0) = 155.3$ mdyne/cm and $\alpha_3^0 = 61.2$ mdyne/(cm K^2).

In a broader temperature range $T < 2$ K, the temperature dependence $\sigma_3(T)$ given by Eqs. (21) and (20) is shown in Fig. 2, where the experimental data obtained in [2, 3] are also presented. To substantiate the ideal fog model, we take the value of density $n_3(T)$ given by Eq. (16) for $T = 1$ K: $n_3(1) = 1.44 \times 10^{14}$ cm^{-2}. Fully saturated (close-packed) fog corresponds to $(n_{03})^{2/3} = 6.5 \times 10^{14}$ cm^{-2}, where n_{03} is the density of liquid He^3. Since $n_3(1) \ll (n_{03})^{2/3}$, the $\lambda_3 = 0$ approximation in Eq. (17) applies, at least, at low temperatures. The model of interest given by Eqs. (20) and (21) does not account for the nonmonotonic $\sigma_3(T)$ dependence at $T \approx 0.1$ K, i.e., for the effects on the order of $\approx 3 \times 10^{-4}$ [4]. For this reason, our model should be improved by introducing Fermi-liquid corrections that were already considered in [12–15]. However, the temperature dependence $\sigma_3(T)$ given by Eq. (2) for high $T > T_F$, where He^3 is a quantum though nondegenerate liquid [8, 9], cannot be explained within the framework of the Fermi-liquid theory.

3. To determine the surface tension $\sigma_4(T)$ of liquid He^4, the contribution $\sigma_S(T)$ from the surface layers

should be separated on the background of ripplon contribution $\sigma_R(T) = -AT^{7/3}$ at $T < 1$ K [5]:

$$\sigma_4(T) = \sigma_4(0) + \sigma_R(T) + \sigma_S(T). \quad (22)$$

Similar to Eqs. (6) and (16), one can determine $\sigma_S(T)$ and $n_4(T)$ [6]:

$$\sigma_S(T) = -T^2 \frac{M_4}{\pi\hbar^2} \int_0^\infty \frac{x\,dx}{\exp\left(x + \frac{\Delta_4}{T}\right) - 1}, \quad (23)$$

$$n_4(T) = -\frac{M_4 T}{2\pi\hbar^2} \ln\left[1 - \exp\left(-\frac{\Delta_4}{T}\right)\right],$$

where M_4 is the effective atomic mass of He^4 and Δ_4 is the surface-level energy measured from the chemical potential μ_4: $\Delta_4 = \varepsilon_4^0 - \mu_4$. The $\mu_4 = \mu_4(T)$ dependence is given by expression (11) with the replacement $C_3 \longrightarrow C_4$. Contrary to $C_3(T)$, the spin contribution to the heat capacity $C_4(T)$ is small, so that one can put $\mu(T) = \mu(0) = -7.15$ K at $T < T_\lambda$. In the ideal fog model, the parameters $\Delta_4 \approx 4$ K and $M_4 \approx 2.6 M_4^0$, where M_4^0 is the He^4 atomic mass, are obtained from the comparison of Eqs. (22) and (23) with the experimental data of [1]. The temperature dependence $\sigma_4(T)$ at $T < T_\lambda$ has the form (Fig. 3)

$$\sigma_4(T) = \sigma_4(0) - AT^{7/3} - \alpha_4^0 T^2 \int_0^\infty \frac{x\,dx}{\exp\left(\frac{\Delta_4}{T} + x\right) - 1}, (24)$$

where $\sigma_4(0) = 354.4$, the Atkins constant is $A = 6.8$, and $\alpha_4^0 = 47$. The corresponding surface-level energy is $\varepsilon_4^0 \approx -3.15$ K.

An intriguing possibility of determining the ripplon contribution to $\sigma_4(T)$ at $T > T_\lambda$ follows from Eqs. (23) and (24) and the data [1] (Fig. 4):

$$-\sigma_R(T) = \sigma_4(0) - \sigma_4(T) + \sigma_S(T). \quad (25)$$

Since the superfluid transition temperature T_λ is not specified for $\sigma_S(T)$, Eq. (23) is valid at $T > T_\lambda$. However, as seen in Fig. 4, the transition through the $T = T_\lambda$ point is highly critical to $\sigma_R(T)$. At $T > T_\lambda$, ripplons are strongly damped because of a high viscosity η of normal He^4. The ripplon damping constant γ can be estimated from the relationship between γ, η, and the fluid density ρ [16]: $\gamma = 2\eta k_T^2/\rho$. The characteristic heat pulse k_T is found from the condition $\hbar\omega(k_T) \approx T$, where
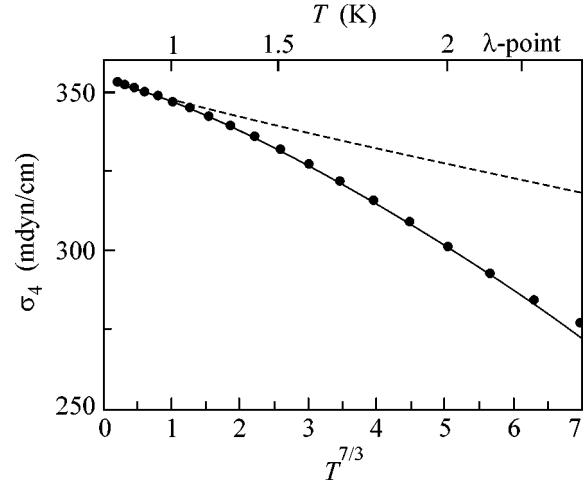

Fig. 3. (Solid line) Temperature dependence of the surface tension σ_4 determined from Eq. (24) for liquid He^4 and (dotted line) the ripplon contribution to $\sigma_4(T)$. Points are the data from [1].
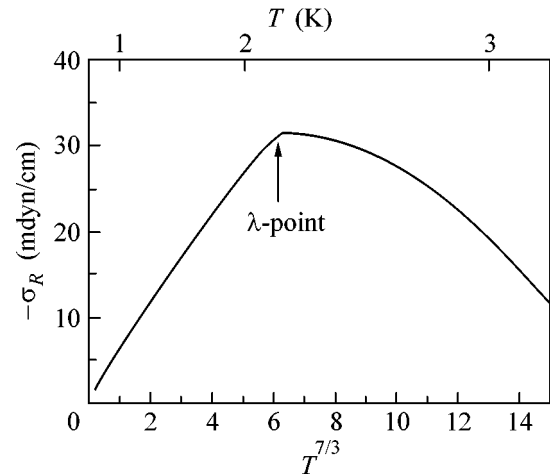

Fig. 4. Ripplon contribution $\sigma_R(T)$ to the surface tension $\sigma_4(T)$, as determined on the basis of Eqs. (23) and (25) and the experimental data from [1].

$\omega^2(k_T) = \sigma k_T^3/\rho$. The smallness $\gamma(k_T) < \omega(k_T)$ is possible if the inequality

$$\frac{2\eta(T)}{\sigma^{2/3}}\left(\frac{T}{\hbar\rho}\right)^{1/3} < 1 \quad (26)$$

is fulfilled.

For He^4, the following criterion follows from Eq. (26):

$$\eta_4(T)T^{1/3} \times 4 \times 10^4 < 1, \quad (27)$$

where η_4 is in g/(cm s). Since $\eta_4(T) > 2 \times 10^{-5}$ for normal He^4, inequality (27) does not hold for He^4 at $T > T_\lambda$.

For liquid He^3, a similar inequality has the form

$$\eta_3(T)T^{1/3} \times 10^5 < 1. \qquad (28)$$

According to the experimental data [17] and the theory [9], the dependence $\eta_3 = \eta_3(T)$ at $T < 2$ K is given by the expression

$$\eta_3(T) = \left(\frac{2.5}{T^2} + 17.5 + \frac{9.4}{T}\right) \times 10^{-6} \text{ g/(cm s)}. \qquad (29)$$

It is seen from Eqs. (28) and (29) that the thermal ripplons in liquid He^3 are strongly damped at all temperatures, and not only at $T \ll T_F$, where $\eta_3(T) \sim 1/T^2$ (29). For this reason, the surface thermodynamics of liquid He^3 is fully governed by the contribution of surface levels at $T < 2$ K (Fig. 2). For liquid He^4, the ripplon contribution to $\sigma_4(T)$ dominates at $T < 1$ K and becomes insignificant at $T > 2.5$ K (Fig. 4). Note that the explanation of the fact that the $\sigma_4 = \sigma_4(T)$ dependence does not fit the Atkins law (1) at $T > 1$ K because of the presence of a roton minimum in the ripplon spectrum [17] is inconsistent with our positions. One can see from Fig. 4 that $\sigma_R \sim T^{7/3}$ for all $T < T_\lambda$.

In conclusion, we have suggested a qualitative theory of surface phenomena in liquid helium. The theory is in a very good agreement with the results of a series of excellent works [1–3] carried out in Japan and explains for the first time the observed temperature dependence of the surface tension of pure isotopes of liquid helium.

REFERENCES

1. M. Iino, M. Suzuki, and A. J. Ikushima, J. Low Temp. Phys. **61**, 155 (1985).

2. M. Iino, M. Suzuki, A. J. Ikushima, and Y. Okuda, J. Low Temp. Phys. **59**, 291 (1985).

3. M. Suzuki, Y. Okuda, A. J. Ikushima, and M. Iino, Europhys. Lett. **5**, 333 (1988).

4. K. Matsumoto, Y. Okuda, M. Suzuki, and S. Misawa, J. Low Temp. Phys. **125**, 59 (2001).

5. K. R. Atkins, Can. J. Phys. **31**, 1165 (1953).

6. L. D. Landau and E. M. Lifshitz, *Course of Theoretical Physics*, Vol. 5: *Statistical Physics*, 3rd ed. (Nauka, Moscow, 1976; Pergamon Press, Oxford, 1980).

7. A. F. Andreev, Zh. Éksp. Teor. Fiz. **50**, 1415 (1966) [Sov. Phys. JETP **23**, 939 (1966)].

8. A. M. Dyugaev, J. Low Temp. Phys. **78**, 79 (1990).

9. A. M. Dyugaev, Sov. Sci. Rev., Sect. A **14**, 1 (1990).

10. K. Shirahama, S. Ito, H. Suto, and K. Kono, J. Low Temp. Phys. **101**, 439 (1995).

11. D. S. Greywall, Phys. Rev. B **27**, 2747 (1983).

12. F. Dalfovo and S. Stringari, J. Low Temp. Phys. **77**, 307 (1989).

13. S. Misawa, J. Low Temp. Phys. **125**, 49 (2001).

14. S. Misawa and H. Morita, Physica B (Amsterdam) **165**, 643 (1990).

15. H. Esbensen and G. F. Bertsch, Phys. Rev. Lett. **52**, 2257 (1984).

16. L. D. Landau and E. M. Lifshits, *Course of Theoretical Physics*, Vol. 6: *Fluid Mechanics*, 5th ed. (Nauka, Moscow, 2001; Pergamon, New York, 1987).

17. L. S. Reut and I. Z. Fisher, Zh. Éksp. Teor. Fiz. **60**, 1814 (1971) [Sov. Phys. JETP **33**, 981 (1971)].

Translated by V. Sakun